The thesis committee for Ravi Ishwar Singh
certifies that this is the approved version of the following thesis:

# Direct Numerical Simulation and Reaction Path Analysis of Titania Formation in Flame Synthesis

APPROVED BY

SUPERVISING COMMITTEE:

Ofodike Ezekoye, Supervisor

Venkat Raman, Supervisor

# Direct Numerical Simulation and Reaction Path Analysis of Titania Formation in Flame Synthesis

**by**

**Ravi Ishwar Singh, B.S.M.E.**

**THESIS**

Presented to the Faculty of the Graduate School of

The University of Texas at Austin

in Partial Fulfillment

of the Requirements

for the Degree of

**MASTER OF SCIENCE IN ENGINEERING**

THE UNIVERSITY OF TEXAS AT AUSTIN

August 2012

Dedicated to my Dad, Mom, and my sister, Indira.

# Acknowledgments

I wish to thank the multitudes of people who helped me. This body of work could not have been produced without the aid of the many great people that I have been fortunate enough to work with.

First, I would like to thank my adviser, Dr. Venkat Raman, who inspired me to pursue the field of computational fluid dynamics (CFD) and who was my mentor during my two years in his research group. In addition to his knowledge, Dr. Raman has also provided me with many opportunities. In the fall, I will attend the International Symposia on Chemical Reaction Engineering and present my research. He also co-wrote a paper with me that has been accepted for publication in the Chemical Engineering Journal. Dr. Raman is a great adviser and leader. I feel truly privileged to have worked in his research group.

I would like to thank Dr. Ofodike Ezekoye for reading my thesis and being my co-adviser. I also had the privilege of taking Dr. Ezekoye's heat transfer class which was very informative and interesting.

I would also like to thank my colleagues in Dr. Raman's Computational Flow Physics Group for their contributions to this research. Dr. Colleen Kaul and Dr. James Sung both helped me with essential parts of the DNS code. I would also like to thank the other members of the research group for their

willingness to answer even my most basic questions about CFD and programming: Dr. Heeseok Koo, Mr. Shaun Kim, Mr. Diogo Lopes, Mr. Pratik Donde, Mr. Colin Heye, Mr. Kalen Braman, Mr. Jaime Martinez, Mr. Chris Lietz, and Mr. Stephen Voelkel. All of these individuals are truly helpful, and I could not have completed this work without their assistance.

Lastly, I would like to thank my Mom, Dad, and my sister Indira. They have always loved me and supported me in everything that I have ever done. Without all that they have done for me, I would not be where I am today.

# Direct Numerical Simulation and Reaction Path Analysis of Titania Formation in Flame Synthesis

Ravi Ishwar Singh, M.S.E.
The University of Texas at Austin, 2012

Supervisors: Ofodike Ezekoye
Venkat Raman

Flame-based synthesis is an attractive industrial process for the large scale generation of nanoparticles. In this aerosol process, a gasified precursor is injected into a high-temperature turbulent flame, where oxidation followed by particle nucleation and other solid phase dynamics create nanoparticles. Precursor oxidation, which ultimately leads to nucleation, is strongly influenced by the turbulent flame dynamics. Here, direct numerical simulation (DNS) of a canonical homogeneous flow is used to understand the interaction between a methane/air flame and titanium tetrachloride oxidation to titania. Detailed chemical kinetics is used to describe the combustion and precursor oxidation processes. Results show that the initial precursor decomposition is heavily influenced by the gas phase temperature field. However, temperature insensitivity of subsequent reactions in the precursor oxidation pathway slow down conversion to the titania. Consequently, titania formation occurs at much longer time scales compared to that of hydrocarbon oxidation. Further, only

a fraction of the precursor is converted to titania, and a significant amount of partially-oxidized precursor species are formed. Introducing the precursor in the oxidizer stream as opposed to the fuel stream has only a minimal impact on the oxidation dynamics. In order to understand modeling issues, the DNS results are compared with the laminar flamelet model. It is shown that the flamelet assumption qualitatively reproduces the oxidation structure. Further, reduced oxygen concentration in the near- flame location critically affects titania formation. The DNS results also show that titania forms on the lean and rich sides of the flame. A reaction path analysis (RPA) is conducted. The results illustrate the differing reaction pathways of the detailed chemical mechanism depending on the composition of the mixture. The RPA results corroborate with the DNS results that titania formation is maximized at two mixture fraction values, one on the lean side of the flame, and one on the rich side.

# Table of Contents

# List of Tables

# List of Figures

# Chapter 1

# Introduction

## 1.1 Motivation

Nanoparticles are particles that have at least one dimension of the order of 100 nm or less. Nanoparticles can be used in a vast array of applications including biotechnology, optics, energy and semiconductors. Although nanoparticles can be produced in many ways, flame synthesis is an attractive method for large scale production of nanoparticles due to its cost effectiveness, scalability, high purity output, and relatively simple single step process [1]. As a result, flame synthesis accounts for the production of close to 90% of commercial nanoparticles [2]. Flame synthesis of nanoparticles has been used in industry since the 1950's, but the process is still not very well understood. Analysis of the process is a challenge due to its complex and strongly interlinked chemical and physical processes which include turbulence, gas phase chemistry, and nanoparticle dynamics. The interaction between these processes covers a wide spectrum of length and time scales. As a result, experiments attempting to optimize the process are based on a trial-and-error approach that is costly, time consuming, and leads to incremental advances at best. However, great advances can be made in the design of flame reactors by creating a reliable and predictive computational model which accurately simulates the flame synthe-

sis process. The model can gain valuable insight into the underlying physical and chemical mechanisms driving the process and be used to develop more efficient designs of reactors. Optimization will lead to higher yields and more precise control over nanoparticle characteristics like particle size, morphology, and composition.

## 1.2 Titania and its Applications

Titania nanoparticles have been used primarily as white pigments for paints, coatings, plastics, and paper in the past. Titania is a commonly used white pigment because of its brightness and high refractive index. $TiO_2$ also has many more industrial uses including photocatalysis [3], surface treatments like anti fog coating [4] and cosmetic applications [5], catalyst supports [6], and ultra-violet blocking materials [7]. Titania has also found usage in many environmental applications. Titania can be used to reduce nitrogen oxide emissions [8] and purify water [9]. They can also be used in the film for dye-sensitized solar cells [10].

### 1.2.1 Market Value of Titania

According to the report *Titanium Dioxide: 2010 World Market Outlook and Forecast* [11], 4 million tons of titania nanoparticles were produced in 2009 with revenues totaling $360 million dollars. Demand for titania is expected to increase with production rates estimated to reach 7.3-7.5 millions tons per year by 2015 with annual revenues expected to reach $1.465 billion

by 2017.

## 1.3 Production of Titania

There are two processes used to manufacture titania nanoparticles, the sulfate process and the chloride process. This report will examine the chloride process, which is the more common technique used to produce titania. 60% of titania is produced by this route currently, and It is estimated that 2015, 66-70% of all titania will be produced by the chloride process [11]. The chloride process for forming purified titania nanoparticles is a multi-step process. First, crude titania (rutile or synthetic beneficiaries containing 90% $TiO_2$) is mined. Next, it is mixed with a source of carbon in a fluidized bed of chlorine at around 900 °C. The ensuing reactions yield titanium tetrachloride, $TiCl_4$, as well as some chlorides of impurities. The mixture is then cooled, and the impurities are separated from the $TiCl_4$ by condensation. Following that, the $TiCl_4$ vapor condenses into a liquid and undergoes and distillation process. The pure $TiCl_4$ is then stored until it is ready to use in flame synthesis.

For the flame synthesis, $TiCl_4$ is fed into a flame reactor, either with the fuel or oxidizer stream. The fuel reacts with the oxidizer quickly causing the fuel to evaporate thereby exposing the precursor ($TiCl_4$) to a high temperature environment in the flame. Here, chloride abstraction occurs for the precursor and the chemical reaction pathways are followed via a series of gas phase reactions to produce nucleated titania nanoparticles. The nucleation of titania is strongly dependent on the background turbulent flow field as well as

the gas phase thermochemical conditions. The nucleated nanoparticles then undergo a surface reactions and collide with other nanoparticles creating clusters called agglomerates (physically bonded) or aggregates (chemically bonded) [12]. Lastly, the final titania nanoparticles are then caught in a collection filter downstream from the reactor.

## 1.4 Prior Studies

Prior experimental studies focusing on titania formation [6] have analyzed the effect of flow conditions on particle characteristics. Typically, a non-premixed diffusion flame configuration is used in these studies. The precursor could be injected along with the fuel or oxidizer. In general, it was found that the specific surface area of the nanoparticle population could be increased by decreasing the time available for aggregation and coalescence (sintering) [13]. This could be achieved by reducing the local precursor concentration, which decreases the nucleation rates and reduces the interaction of particles. Alternatively, the flow rates could be increased to reduce the residence time of the particles in the high-temperature region. For instance, it was found [6] that an increase in the air flow rate increased the particle velocities, leading to reduced time in the post-flame region.

To capture these effects in a computational model, a comprehensive description of both gas phase precursor evolution and solid phase nanoparticle evolution is necessary. Here, the focus is on the gas phase precursor oxidation that dictates the spatial distribution of solid particle nucleation relative to

the turbulent flame location. The evolution of particles is highly dependent on the background turbulent flow field, and the gas phase thermochemical conditions. In this sense, the nucleation location serves as an initial condition for the particle trajectories in physical space.

Precursor oxidation is sensitive to temperature and local oxygen concentration [14, 15]. A hierarchy of chemistry models have been used to describe this oxidation process [14, 16–19]. A study by [16] used an instantaneous nucleation assumption, where the precursor was assumed to be completed converted to the oxide if the local temperature exceeds a critical value, $T_d$, set to 340 K [16] . Here, nucleation occurs at sufficiently large distance from the diffusion flame. It was also found that the simulations were relatively insensitive to the nucleation temperature ($T_d$). A one-step chemistry mechanism that takes into account precursor consumption through surface growth has also been formulated [14, 17]. More recently, a detailed multi-step chemistry mechanism has been developed [20–22]. While these mechanisms were predominantly developed for precursor oxidation in high-temperature air, [15] and [22] extended the detailed mechanism to precursor oxidation in methane-air flames. Although the detailed mechanisms have not been thoroughly validated due to the lack of high-fidelity measurements, [23] showed that the use of the detailed mechanism reproduces the particle evolution observed in experiments quite accurately, without having to tune any other model constants.

# Chapter 2

# Two-dimensional DNS of Titania Nucleation with Detailed Chemistry

In this chapter, the flow configuration and the numerical approach for solving the governing equations are described. A spectral approach is used for solving the governing equations in a periodic flow domain.

## 2.1 Flow Configuration and Governing Equations

In DNS, the Navier-Stokes equations are solved without any model used for turbulent motion. All length and time scales of turbulence are resolved fully in DNS which leads to greater accuracy of the solution at the expense of computational time. A two-dimensional periodic (in both directions) square domain of length 36 mm is used. This length is chosen so that the range of length scales associated with turbulence is close to the smallest reaction-associated length scale. The turbulent flow is homogeneous and isotropic inside this flow configuration. An initialized segregated fuel-air system laden with precursor material then evolves in this turbulent flow. Due to viscous dissipation, the turbulent fluctuations will decay with time. Since scalar mixing is also irreversible, this system represents an unsteady evolution

of a diffusion flame. A similar flow configuration has been used previously to study soot formation in flames [24]. The flow field evolves as follows:

$$\frac{\partial u_i}{\partial t} + \frac{\partial u_i u_j}{\partial x_j} = -\frac{\partial p}{\partial x_i} + \nu \frac{\partial^2 u_i}{\partial {x_j}^2}, \tag{2.1}$$

where $u_i$ is the velocity in the $i$-th direction, $p$ is the pressure, $\nu$ is the kinematic viscosity, and summation is implied for repeated indices. The density is assumed to be constant and equal to 1 in this flow. The continuity equation is given by

$$\frac{\partial u_j}{\partial x_j} = 0. \tag{2.2}$$

In incompressible flow, the pressure term in the velocity equation only acts to enforce the continuity equation [25]. The gas phase oxidation of precursor and combustion of fuel is represented using a $N$-species thermochemical system (including temperature). The transport equations for these scalars is written as

$$\frac{\partial \phi_\alpha}{\partial t} + \frac{\partial u_j \phi_\alpha}{\partial x_j} = D \frac{\partial^2 \phi_\alpha}{\partial x_j^2} + \dot{\omega}_\alpha(\boldsymbol{\phi}), \tag{2.3}$$

where $\phi_\alpha$ is the mass fraction of the $\alpha$-th species, $D$ is the diffusivity, $S_\alpha$ is the chemical source term that depends on the entire thermochemical composition vector $\boldsymbol{\phi} = \{\phi_1, \phi_2, \cdots, T\}$. Here, the diffusivities of the scalars as well as the Lewis number are assumed to be equal. In order to fully describe the multi-step oxidation of fuel and precursor, the detailed chemical mechanism developed by [15] is used here. This mechanism for titanium tetrachloride oxidation in methane-air flames consists of 47 species (including temperature) and 162 reactions. The mechanism can be seen in Appendix A.

## 2.2 Quasi-Spectral Numerical Approach

The two-dimensional time-varying velocity and scalar fields are transformed intro spectral space using a Fourier-transform and solved [25]. This transform from physical to spectral space is given by equation 2.4.

$$\widehat{\psi}(k_x, k_y, t) = \frac{1}{N_1}\frac{1}{N_2}\sum_{i=0}^{N_1}\sum_{j=0}^{N_2}\psi(x_i, y_j, t)e^{-ik_x x_i}e^{-ik_y y_j}, \tag{2.4}$$

where $\widehat{\psi}$ is the transformed field corresponding to the physical-space field $\psi$, $k_x$ and $k_y$ are the coordinates in wavenumber space, and $N$ (for $N_1$ and $N_2$) refers to the number of wavemodes used to discretize the wavenumber space. $N$ controls the range of length scales that could be evolved, implying that a higher value is required with increase in the Reynolds number. The simplified Navier-Stokes equations for this study are given by equation 2.5

$$\frac{\partial u_i}{\partial t} + H_i = \nu\frac{\partial^2 u_i}{\partial {x_j}^2} \tag{2.5}$$

where $H_i$ is the nonlinear convection term which is solved in skew-symmetric form and is given by equation 2.6. The skew-symmetric form is used to minimize aliasing errors [26]. Mass conservation implied by the continuity equation (Eq. 2.2) is enforced by the pressure term through an elliptic equation [27].

$$H_i = \frac{1}{2}\left(\frac{\partial u_i u_j}{\partial x_j} + u_j\frac{\partial u_i}{\partial x_j}\right) \tag{2.6}$$

The Navier-Stokes equations were then Fourier-transformed into spectral space. The Fourier transform of each term is given by the equations below.

$$\mathcal{F}\left(\frac{\partial u_i}{\partial t}\right) = \frac{\partial \hat{u}_i}{\partial t} \tag{2.7}$$

$$\mathcal{F}\left(H_i\right) = \hat{H}_i = \frac{1}{2}\left[ik_j(\widehat{u_i u_j}) + \left(u_j \widehat{\mathcal{F}^{-1}(ik_j \hat{u}_i)}\right)\right] \tag{2.8}$$

$$\mathcal{F}\left(\nu \frac{\partial^2 u_i}{\partial^2 x_j}\right) = -\nu k^2 \hat{u}_i \tag{2.9}$$

where $k^2 = k_x^2 + k_y^2$. Putting the transformed terms together leads to equation 2.10.

$$\frac{\partial \hat{u}_i}{\partial t} + \nu k^2 \hat{u}_i = -\hat{H}_i \tag{2.10}$$

Next, equation 2.10 was multiplied by $e^{\nu k^2 t}$ to yield equation 2.12.

$$e^{\nu k^2 t}\left[\frac{\partial \hat{u}_i}{\partial t} + \nu k^2 \hat{u}_i\right] = e^{\nu k^2 t}\left[\hat{H}_i\right] \tag{2.11}$$

$$\frac{\partial \hat{u}_i e^{\nu k^2 t}}{\partial t} = \hat{H}_i e^{\nu k^2 t} = f(u_i, t) \tag{2.12}$$

To advance the solution forward in time, a second-order Runge-Kutta scheme was used with a predictor step followed by a corrector step as shown by equations 2.13 and 2.14 [28].

$$\hat{u}_i(t + \frac{\Delta t}{2}) = \left(\hat{u}_i(t) + \frac{\Delta t}{2}\hat{H}_i\right) e^{-\nu k^2 \frac{\Delta t}{2}} \tag{2.13}$$

$$\hat{u}_i(t + \Delta t) = \left(\hat{u}_i(t) + \Delta t \hat{H}_i\right) e^{-\nu k^2 \Delta t} \tag{2.14}$$

For the first step, the nonlinear term is evaluated using the initial velocity values at time $t$. For the second step, the nonlinear term uses the velocity values calculated from the first step.

To simulate the combustion, the scalar transport equation was also advanced spectrally in time for temperature, mixture fraction, and the mass fraction of each of the 46 species. In total, 50 equations were solved at each

time step (48 scalars and the 2 momentum equations). The scalar transport equation (in real space) is given by equation 2.15.

$$\frac{\partial \phi_\alpha}{\partial t} + H_\alpha = D\frac{\partial^2 \phi_\alpha}{\partial^2 x_j} \tag{2.15}$$

where $H_\alpha$ contains the nonlinear term as well as the chemical source term of the $\alpha$-th species as shown in equation 2.16. For the scalars, the nonlinear term was solved in non-conservative form.

$$H_\alpha = u_j \frac{\partial \phi_\alpha}{\partial x_j} - \dot{\omega}_\alpha \tag{2.16}$$

Transforming the terms of equation 2.15 into spectral space and following the same procedure as for the Navier-Stokes equations, leads to equations 2.17 and 2.18.

$$\hat{\phi}_\alpha(t + \frac{\Delta t}{2}) = \left(\hat{\phi}_\alpha(t) + \frac{\Delta t}{2}\hat{H}_\alpha\right) e^{-Dk^2\frac{\Delta t}{2}} \tag{2.17}$$

$$\hat{\phi}_\alpha(t + \Delta t) = \left(\hat{\phi}_\alpha(t) + \Delta t\hat{H}_\alpha\right) e^{-Dk^2\Delta t} \tag{2.18}$$

Like with the fluid flow equations, the nonlinear term is evaluated with the initial scalar and velocity values for the first step, and with the values from the predictor step for the second step. However, the source term must be updated for each step as well.

The chemical source terms appearing in the scalar transport equation ($\dot{\omega}_\alpha$ in Eq. 2.3) are inherently stiff due to the large separation of time scales associated with the different reactions in the chemical mechanism. In an explicit time-stepping algorithm, the local time-step will then be determined by the smallest time-scale, which will make the computations prohibitively expensive.

To overcome this numerical difficulty, a time-splitting technique is used. At each time-step, the scalar field at the beginning of the step is denoted by $\boldsymbol{\phi}^n$. Using a stiff ODE integrator (DDASAC, [29]), the following equation is solved at each grid point:

$$\boldsymbol{\phi}^* = \int_0^{\Delta t} \mathbf{S}(\boldsymbol{\phi}) dt, \tag{2.19}$$

where $\boldsymbol{\phi}^*$ is the solution after time-step $\Delta t$, and $\mathbf{S} = \{S_1, S_2, \ldots, S_T\}$, is the vector of source terms. The time-step $\Delta t$ is determined based on a CFL condition obtained using the velocity field. Based on this solution, a new source term is obtained as follows:

$$\mathbf{S}^* = \frac{\boldsymbol{\phi}^* - \boldsymbol{\phi}^n}{\Delta t}. \tag{2.20}$$

This source term is assumed to be constant during the time-step, transformed to spectral space, and added to the scalar transport equation. Specifically, the temperature is advanced in time in the stiff ODE solver by solving equation 2.21 which is derived from the energy equation [30].

$$\frac{dT}{dt} = \frac{-\sum_{\alpha=1}^{n} h_\alpha \dot{\omega}_\alpha MW_\alpha}{\rho c_p} \tag{2.21}$$

for $n$ species, where $h_\alpha$ is enthalpy of the specie, $MW_\alpha$ is the molecular weight of the specie, and $\rho$ and $c_p$ are the density and specific heat of the mixture. The mixture fraction has no source term in its transport equation, so it did not need to be integrated. The mass fraction of each species was integrated in time by using equation 2.22 [30].

$$\frac{dY_\alpha}{dt} = \frac{\dot{\omega}_\alpha MW_\alpha}{\rho}, \alpha = 1 \ldots n \tag{2.22}$$

As the temperature and mass fractions are integrated over the timestep, the chemical source term evolves. After integrating the scalars within the flow time step, the updated source terms are then put back into the nonlinear term in the Runge-Kutta transport equation to be used in calculating the scalar at the next time step.

A variable timestep was used for the Runge-Kutta method that depended on the velocity field as well as the kinematic viscosity of the mixture. The timestep was calculated using equation 2.23

$$\Delta t = min\left(\frac{C\Delta x}{max(U)}, \frac{C\Delta x}{max(V)}, \frac{\Delta x^2}{2\nu}\right) \tag{2.23}$$

where C is the Courant number which was given a value of 0.2 for this simulation.

## 2.3 Flow Initialization and Flamelet Mapping

### 2.3.1 Flow Initialization

The flow conditions are chosen to closely mimic the turbulent jet experiment of [6], in particular the flame D configuration. The flow is initialized by prescribing a turbulent velocity field with specified conditions. The scalar field is chosen to represent a segregated fuel/air system that mixes in this turbulent background flow. Table 1 shows the initial conditions used to specify the turbulent flow. The Taylor-scale Reynolds number is set to 50 and closely corresponds to the jet Reynolds number used in the experiment. Similarly, the turbulence time scale ($\tau = L_{11}/u'$) of 11 ms is roughly equal to the timescale

computed based on the jet diameter and velocity.

| Parameter | Symbol | Value |
|---|---|---|
| Domain length | L (mm) | 36 |
| Integral length scale | $L_{11}$ (mm) | 3.5 |
| Number of grid points | $N_x$ x $N_y$ | 512 x 512 |
| Grid spacing | $\Delta x, \Delta y$ ($\mu m$) | 70 |
| RMS velocity fluctuation | u' ($\frac{m}{s}$) | 0.32 |
| Kolmogorov length scale | $\eta$ ($\mu m$) | 220 |
| Kolmogorov time scale | $\eta_T$ (ms) | 3 |
| Taylor-scale Reynolds number | $Re_\lambda$ | 50 |
| Jet Reynolds number | $Re_\tau$ | 375 |
| Turbulence time scale | $\tau$ (ms) | 11 |
| Fuel strip width | $h_z$ (mm) | 6 |
| Mixing layer width | $\delta_z$ (mm) | 2 |

Table 2.1: Turbulence parameters.

In order to provide a turbulent field with prescribed length and time scales, a theoretical energy spectrum is used. The Passot-Pouquet spectrum [31] gives the turbulent energy content as a function of wavenumber.

$$E(\kappa) = \frac{32}{3}\sqrt{\frac{2}{\pi}}\frac{u'^2}{\kappa_e}\left(\frac{\kappa}{\kappa_e}\right)^4 exp\left[-2\left(\frac{\kappa}{\kappa_e}\right)^2\right], \tag{2.24}$$

where $u'$ is the root-mean-square velocity fluctuation in the domain, $k$ is the wavenumber obtained from the wavenumber coordinates ($k = \sqrt{k_x^2 + k_y^2}$), and

$k_e$ is the most energetic wavenumber obtained as follows [32]:

$$\kappa_e = \sqrt{\frac{4\epsilon}{10\nu u'^2}}. \tag{2.25}$$

The energy spectrum is transformed into the Fourier modes for the velocity field using the method formulated by Rogallo [33]. Figure 2.1 shows the x-component of the velocity field obtained using this spectrum. As the flow evolves, the time scales will change but it was observed that the Reynolds number, which is proportional to the ratio of large to small time scale, was found to change minimally.

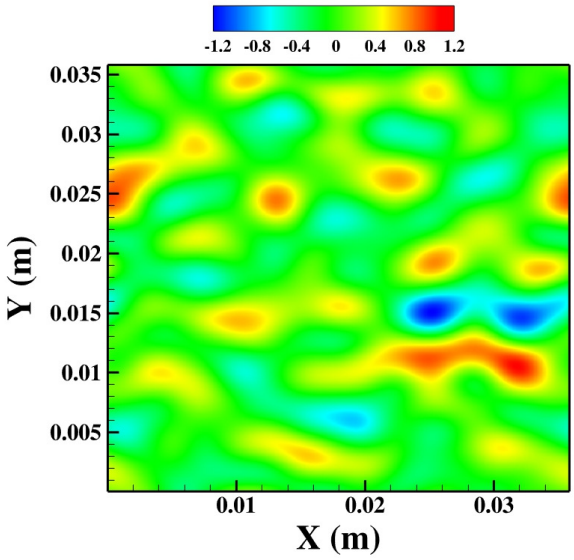


Figure 2.1: Initial velocity field (m/s).

### 2.3.2 Flow Composition

Two different precursor injection conditions are considered. In the first case, termed the normal flame, the precursor and Argon gas are injected along with the fuel. In the second case, termed the inverse flame, the precursor and Argon are present in the oxidizer stream. These cases correspond to the Flame D and A configurations of [6], respectively. The composition of the fuel and oxidizer streams for the two cases are provided in Table 2.

| | Normal Flame | Inverse Flame |
|---|---|---|
| $Z_{st}$ | 0.167 | 0.056 |
| Species | Mass Fraction | Mass Fraction |
| $CH_4$ | 0.278 | 1.000 |
| $TiCl_4$ | 0.167 | 0.025 |
| Ar | 0.555 | 0.081 |
| $O_2$ | 0.233 | 0.208 |
| $N_2$ | 0.767 | 0.686 |

Table 2.2: Stream compositions.

### 2.3.3 Flamelet Mapping

The scalars are initialized in a two-step procedure. In the first step, a conserved scalar termed mixture fraction ($Z$) is defined such that it is set to 1 in the fuel stream and 0 in the oxidizer stream. This scalar is initialized using the following function [32], leading to the spatial distribution shown in

Fig. 2.2:

$$Z(x) = \frac{1}{4}\left(1 + \tanh\left[\frac{L + h_z + \delta_z - 2x}{\delta_z}\right]\right)\left(1 + \tanh\left[\frac{-L + h_z + \delta_z + 2x}{\delta_z}\right]\right). \tag{2.26}$$

In the second step, the species and temperature profiles in the domain are

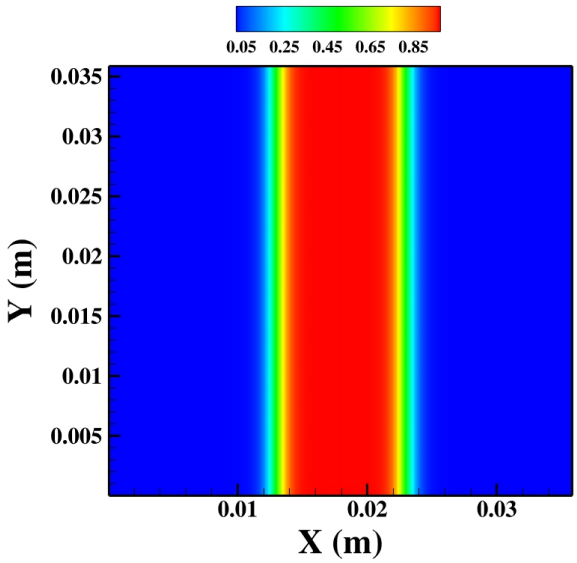


Figure 2.2: Initial mixture fraction profile.

imposed using the solution to the one-dimensional laminar flamelet equations [34]. Here, the following the reactive-diffusive equation is solved in mixture fraction space.

$$\frac{\chi}{2}\frac{\partial^2 \phi_\alpha}{\partial Z^2} + S_\alpha = 0, \tag{2.27}$$

where $\chi$ is the scalar dissipation rate defined as

$$\chi = 2D\frac{\partial Z}{\partial x_j}\frac{\partial Z}{\partial x_j}. \tag{2.28}$$

The boundary conditions (at $Z = 1$ and $Z = 0$) are based on the fuel and oxidizer stream inflow conditions. The solution to this equation then provides the species compositions and temperature in terms of mixture fraction and scalar dissipation rate.

$$\phi_\alpha = \mathcal{H}(Z, \chi), \tag{2.29}$$

where $\mathcal{H}$ denotes the flamelet mapping obtained by the solution to Eq. 2.27. The flamelet equations are solved *a priori* and the results stored in the form of a lookup table. Mixture fraction and the dissipation rate (computed from the $Z$ field) are then used to lookup the species compositions and imposed as the initial field for the DNS computation. Figure 2.3 shows a sample flamelet solution for temperature evaluated for a single dissipation rate. The laminar

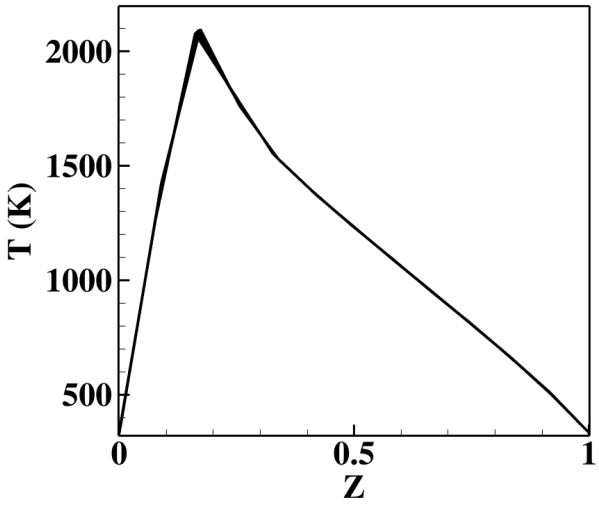


Figure 2.3: Flamelet temperature versus mixture fraction for a scalar dissipation rate of $\chi = 0.05$.

flamelet mapping invokes a number of assumptions [34, 35]. The most critical of which is that the reaction zone is confined to a very thin region in physical space, smaller than the Kolmogorov length scale. Consequently, turbulence affects only large scale mixing of oxidizer and fuel, but does not penetrate the reaction zone. The effect of turbulence on the flame is felt through the dissipation rate, which provides a diffusion time scale. If the dissipation rate is high, the diffusion of heat from the reaction zone will quench the flame leading to extinction. In typical combustion processes far from extinction, the reactions are fast enough for these assumptions to be valid. The pre-tabulation of chemical composition vastly reduces the computational cost associated with large chemistry mechanisms. In this sense, the laminar flamelet model is an extraordinarily effective means of utilizing detailed chemistry models in high-fidelity CFD computations. For this reason, one of the objectives in the analyses presented below is to understand whether this one-dimensional model could be used to describe precursor oxidation in the presence of a flame. By initializing the domain from a flamelet solution, the departure of the species compositions from this manifold could be studied.

# Chapter 3

# Direct Numerical Simulation Results

Two different flame configurations (normal and inverse) were studied. In the normal flame, the precursor is present in the fuel stream while for the inverse flame, the precursor is present in the oxidizer stream. Since precursor oxidation requires access of oxygen atoms, which are also being actively consumed by the hydrocarbon combustion process, the focus here is in determining whether there are key differences in the precursor/flame structure for the two configurations.

## 3.1 Normal Flame Configuration

Figure 3.1 shows the evolution of mixture fraction with time for the normal flame. All of the contour plots show a reduced domain with only one flame front in order to facilitate the viewing of minute details of the flame. The turbulent flow increases the surface area available for mixing, leading to increased molecular diffusion. As time progresses, the gradient of mixture fraction on either side of the stoichiometric line decreases. This implies that scalar dissipation rate will also decrease with time. Note that in the limit of zero scalar dissipation rate, Eq. 2.27 will revert to chemical equilibrium.

Figure 3.2 shows the evolution of the temperature field with time. At early times, the flamelet-based initial conditions keep the high temperature zone very close to the stoichiometric line. However, even at later times, the highest temperature is observed very close to the stoichiometric line.

To understand the departure from the flamelet manifold, it is instructive to look at the scatter plots of species and temperature plotted against mixture fraction. Figure 3.3 shows the conditional plot of temperature, as well as OH and $O_2$ mass fractions at time $t = \tau$. It can be seen that both these quantities closely follow the flamelet solution at later times as well, indicating that the associated assumptions are valid for this flow configuration. Note that the scatter in the flamelet solution seen in the plots arise from the variations in the local scalar dissipation rate.

Figure 3.4 shows the evolution of the titania mass fraction as a function of time. Unlike temperature and other gas phase species discussed before, titania mass fractions increase locally with time. However, after $t = \tau$, the titania mass fraction shows no significant departure from the flamelet manifold. Figure 3.5 shows the conditional scatter plot along with the flamelet solution for select Ti-containing species in the gas phase. For this configuration, the titania mass fraction is closely predicted by the flamelet model. As will be discussed below, this close agreement is predominantly due to the low conversion yield. If all of the titanium tetrachloride were to be converted to titania, this irreversible reaction will definitely not follow the flamelet solution. However, there is a large scatter in the titania mass fraction for a given

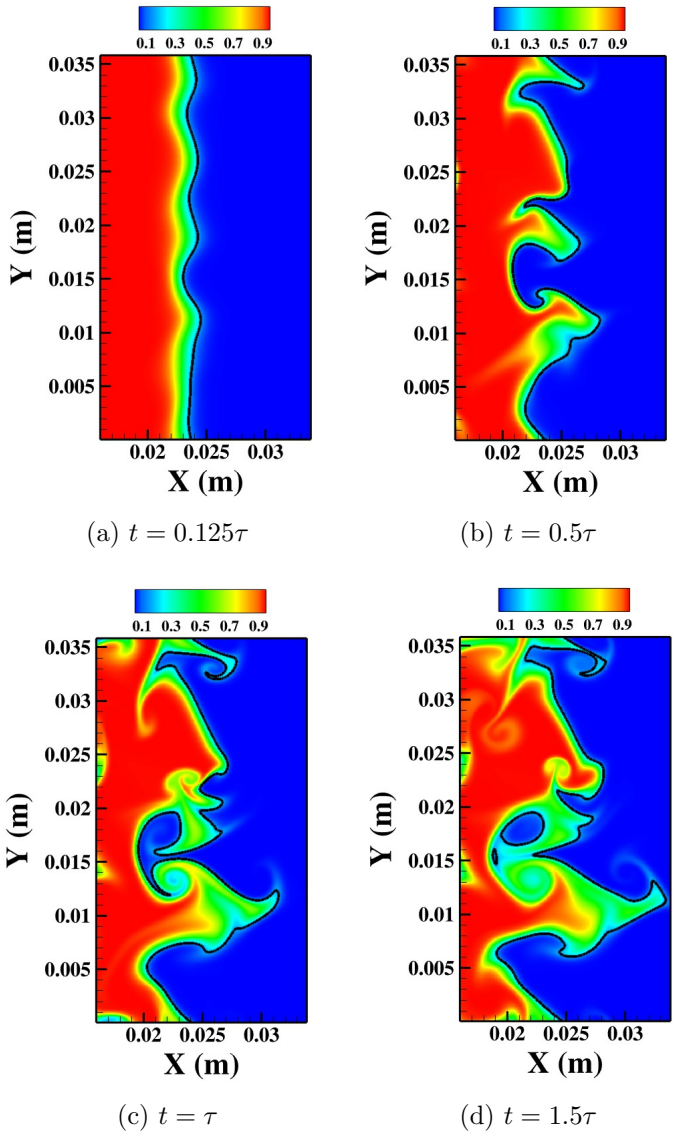


(a) $t = 0.125\tau$ (b) $t = 0.5\tau$

(c) $t = \tau$ (d) $t = 1.5\tau$

Figure 3.1: Contour plots of mixture fraction for the normal flame (stoichiometric mixture fraction ($Z_{st} = 0.167$) plotted as a black line).

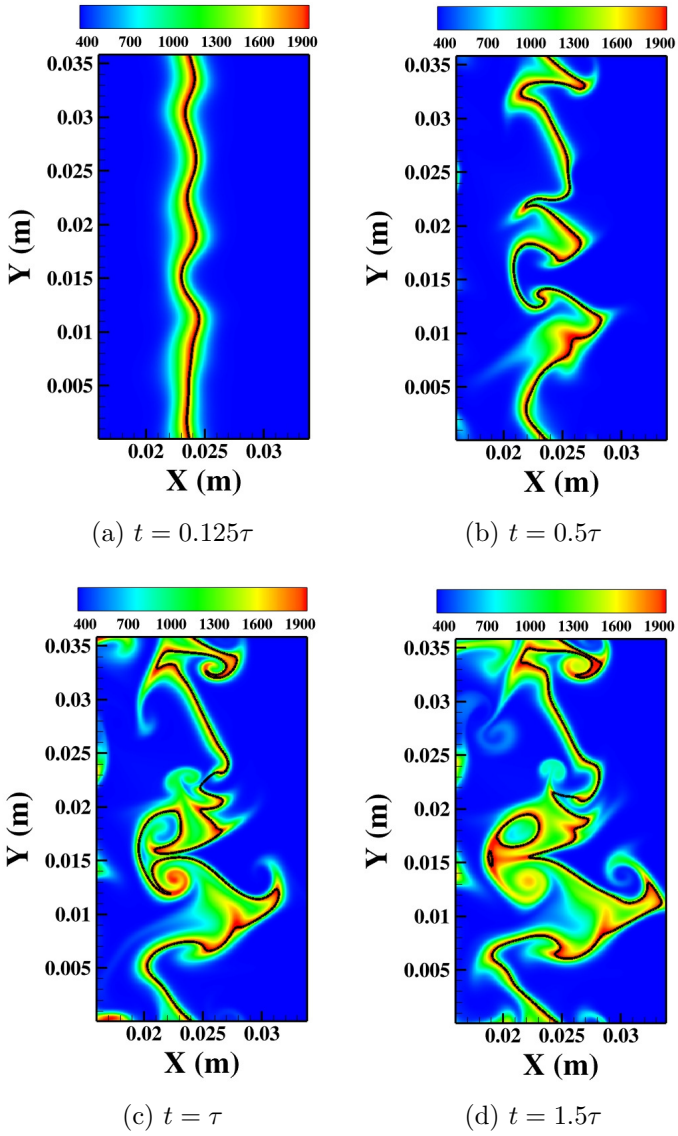


(a) $t = 0.125\tau$ (b) $t = 0.5\tau$

(c) $t = \tau$ (d) $t = 1.5\tau$

Figure 3.2: Contour plots of temperature (in K) for the normal flame (stoichiometric mixture fraction ($Z_{st} = 0.167$) plotted as a black line).

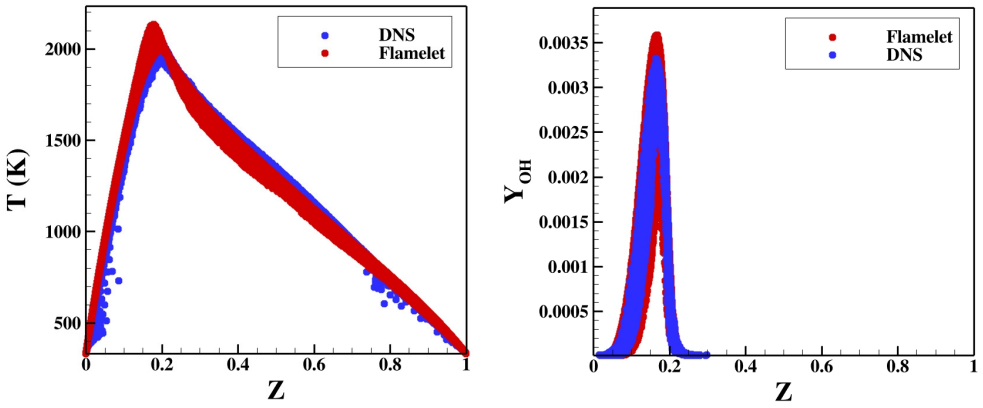


(a) Temperature




(b) OH

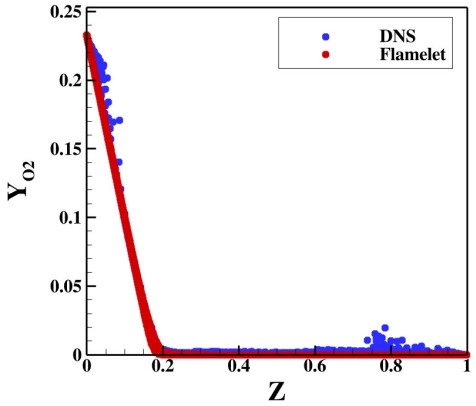


(c) $O_2$

Figure 3.3: Comparison of flamelet and DNS values for the normal flame at $t = \tau$.

mixture fraction, which is not present in the temperature or oxygen conditional scatter plot. Note that single-step oxidation mechanisms directly relate temperature and oxygen concentration to the precursor oxidation rate. In this

sense, the multi-step mechanism shows a more complex relation with respect to temperature and oxygen.

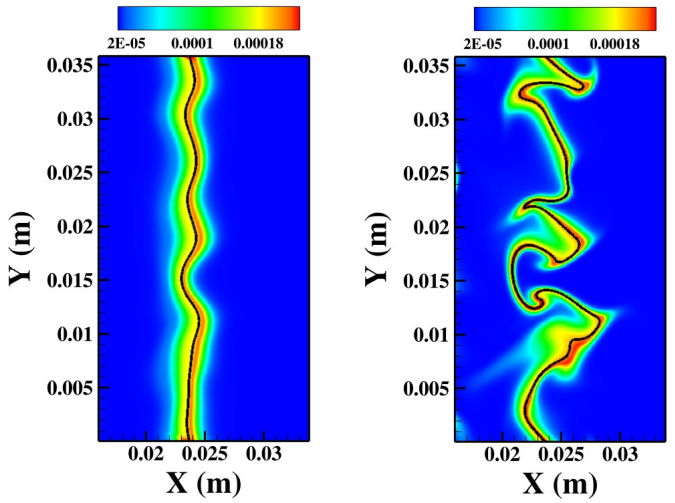


(a) $t = 0.125\tau$ (b) $t = 0.5\tau$

(c) $t = \tau$ (d) $t = 1.5\tau$

Figure 3.4: Contour plots of mass fraction of $TiO_2$ for the normal flame (stoichiometric mixture fraction ($Z_{st} = 0.167$) plotted as a black line).

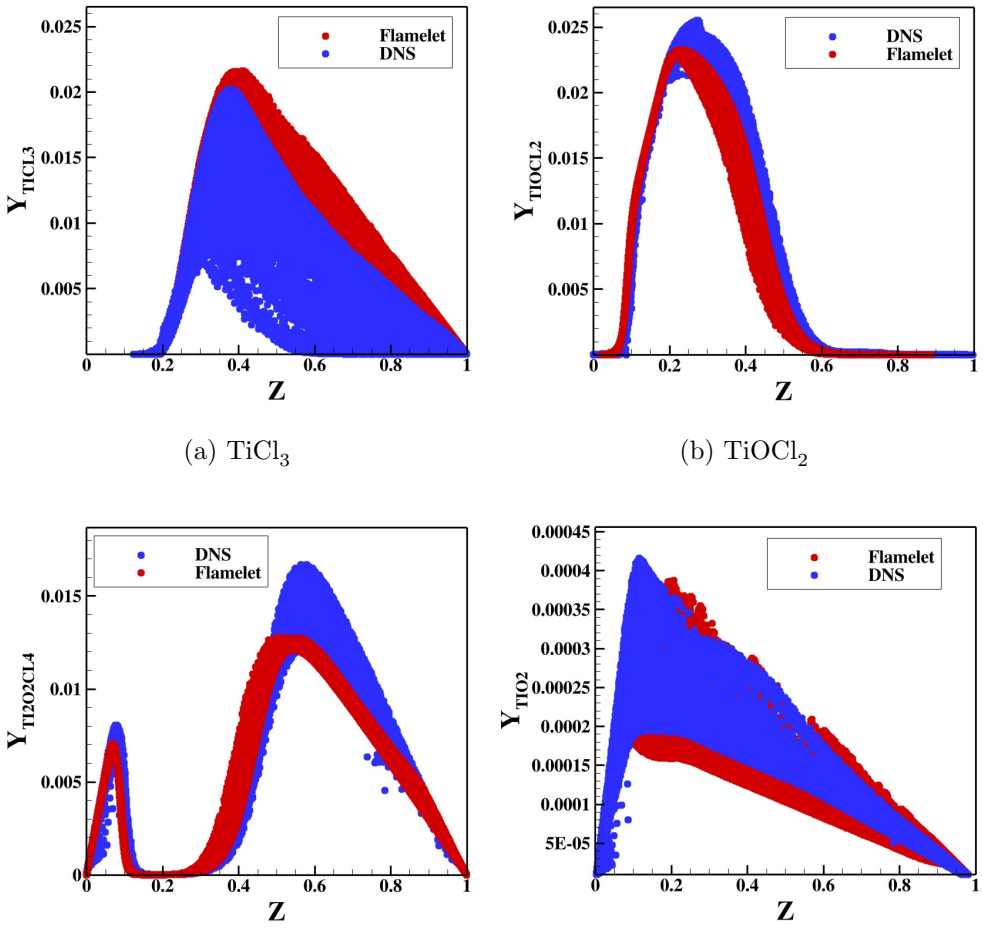


(a) $TiCl_3$ (b) $TiOCl_2$

(c) $Ti_2O_2Cl_4$ (d) $TiO_2$

Figure 3.5: Comparison of flamelet and DNS values for the normal flame at $t = \tau$.

To further understand the titania evolution process, conditional plots of key species are shown in Fig. 3.5. The titanium tetrachloride precursor first breaks down into $TiCl_3$, which then initiates different pathways for conversion

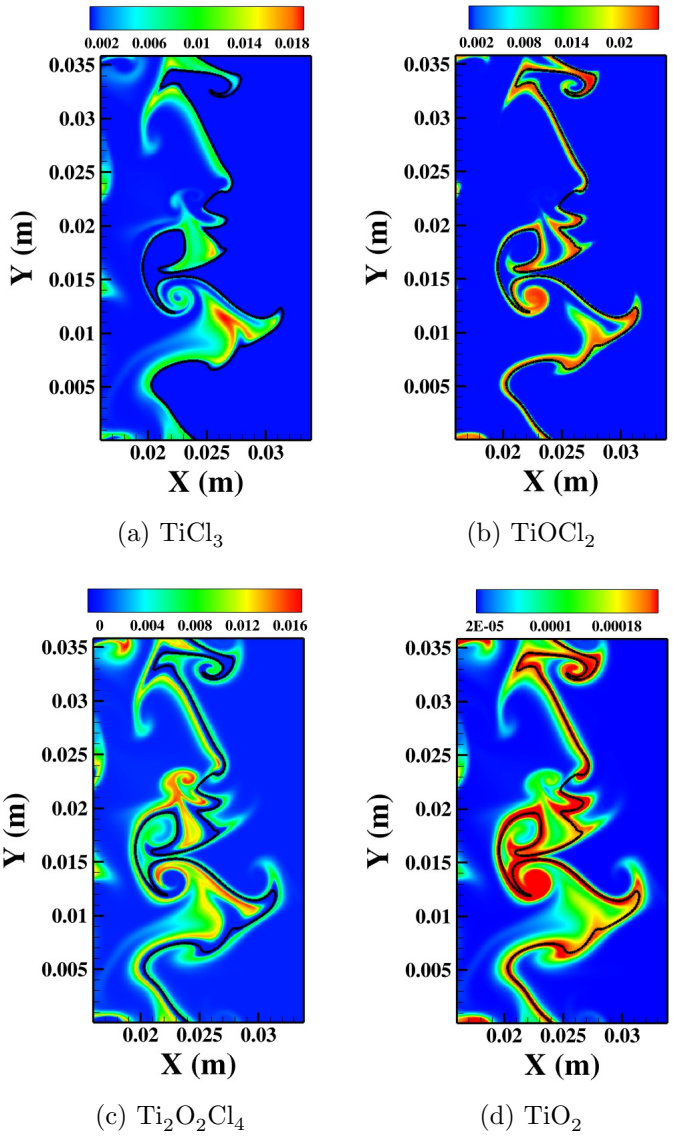


(a) $TiCl_3$ (b) $TiOCl_2$

(c) $Ti_2O_2Cl_4$ (d) $TiO_2$

Figure 3.6: Contour plots of Ti-species for the normal flame at $t = \tau$.

to titania. In addition to titania, $TiOCl_2$ and $Ti_2O_2Cl_4$ appear in appreciable quantities. In the mechanism used here, only a few reactions associated with

the Ti species are sensitive to temperature (i.e., non-zero activation and temperature exponent in the Arrhenius rate expression). In particular, the final reactions that produce titania are driven primarily by the concentration of the species involved rather than the local temperature. This feature is observed in the conditional plots (Fig. 3.5). The decomposition reaction of titanium tetrachloride is temperature dependent, but is activated at relatively low temperatures. More importantly, there is large scatter in data indicating that for a given mixture fraction, the level of decomposition is extremely sensitive to local conditions as well as residence time in a particular gas phase environment. It is also seen that the decomposition to $TiCl_3$ occurs completely on the rich side of the flame.

The formation of the stable monomer, $TiOCl_2$, is dominant close to stoichiometric conditions (Fig. 3.6b). Unlike precursor decomposition, the formation of the monomer species extends to either side of the stoichiometric mixture fraction. Since the monomer formation involves a reaction with either oxygen molecule or a oxygen radical, this process directly competes with the hydrocarbon oxidation process. Since oxygen is depleted on the rich side, the formation of monomer on the lean side indicates that some of the precursor material diffuses relative to the flame location onto the oxidizer-rich lean side. The conditional scatter plot of the dimer, $Ti_2O_2Cl_4$ (Fig. 3.5c), exhibits two peaks on either side of the stoichiometric mixture fraction. The dimerization is solely driven by monomer formation. The two peaks indicate that the rate of dimerization is slow compared to the rate of formation of the monomer, and

that diffusion of monomer away from the flame location takes place prior to dimerization. Figure 3.6 shows contour plots of $TiCl_3$, $TiOCl_2$ and $Ti_2O_2Cl_4$ mass fractions. It is clear that the initial precursor decomposition occurs close to the flame location, but is significantly active even further away on the fuel-rich side of the flame. The monomer distribution resembles titania mass fraction, with peak values observed along the stoichiometric surface. However, the dimer concentration peaks at locations further away, indicating a slower process compared to monomer formation.

The formation of titania molecules proceeds through a set of steps starting with the formation of the monomer. Interestingly, the results indicate that titania is not the main product that is formed, and is in fact produced in very small quantities compared to the stable monomer and dimer species. Unlike single-step mechanisms that provide complete oxidation, the multi-step chemical mechanism appears to indicate a very low yield from this precursor. The conversion of monomer to titania requires the formation of Ti-species with at least 3 Ti atoms, which are formed in very small quantities. The scatter seen in the conditional plots for the initial decomposition of the precursor ($TiCl_3$ in Fig. 3.5a), combined with the slow formation of the dimer leads to the scatter in the the titania mass fraction conditional plot (Fig. 3.5d) as well. Titania is also formed on either side of the stoichiometric surface (Fig. 3.6d), consistent with the diffusive-transport of monomer and the formation of the dimer.

## 3.2 Inverse Flame Configuration

In the inverse flame configuration, the precursor is mixed with the oxidizer stream. Figure 3.7 shows the time evolution of mixture fraction, while Figure 3.8 shows the contour plot of temperature for this case. The stoichiometric mixture fraction is much lower compared to the normal flame configuration. As expected, temperature peaks close to the stoichiometric surface. The gas phase species were found to follow the flamelet solution similar to the normal flame, and is not shown here. Figure 3.9 shows the evolution of titania mass fraction for this inverse flame configuration. Titania mass fraction is seen to peak at slightly leaner mixture fraction compared to the stoichiometric value, but it is present on both sides of the flame surface. The conditional scatter plot of titania mass fraction (Fig. 3.10d) shows that the flamelet solution closely predicts titania formation, which is similar to the results observed in the normal flame configuration. To further probe the oxidation pathway, the conditional scatter plots of Ti-containing species are also shown in Figure 3.10. The most important difference from the normal flame configuration is the relatively low mass fraction of $TiCl_3$ in the inverse flame configuration. Since precursor decomposition is driven only by temperature and can occur at relatively low temperatures, $TiCl_3$ is formed on the lean side. However, the presence of excess oxygen causes direct oxidation leading to monomer and dimer formation. In the normal flame configuration, $TiCl_3$ had to compete with the hydrocarbons for oxygen on the rich side, which caused a delay in the formation of the monomer and dimer. In that sense, the inverse flame

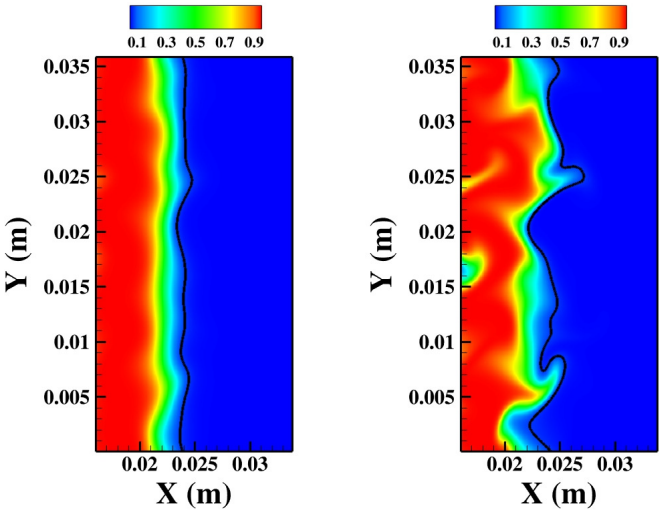


(a) $t = 0.125\tau$ (b) $t = 0.5\tau$

(c) $t = \tau$ (d) $t = 1.5\tau$

Figure 3.7: Contour plots of mixture fraction for the inverse flame (stoichiometric mixture fraction ($Z_{st} = 0.056$) plotted as a black line).

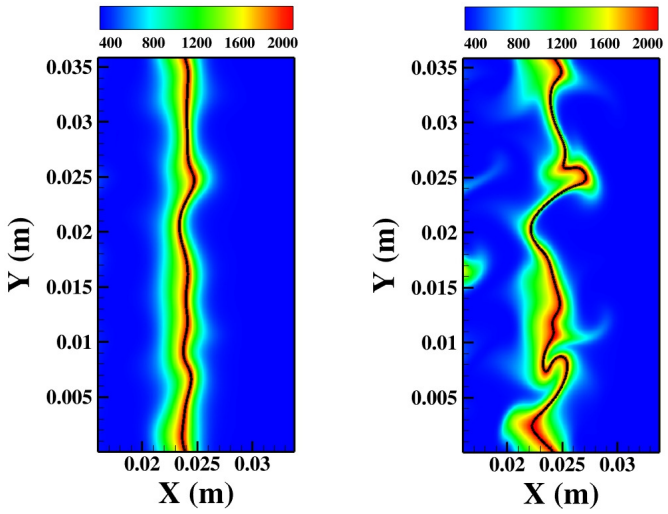


(a) $t = 0.125\tau$




(b) $t = 0.5\tau$

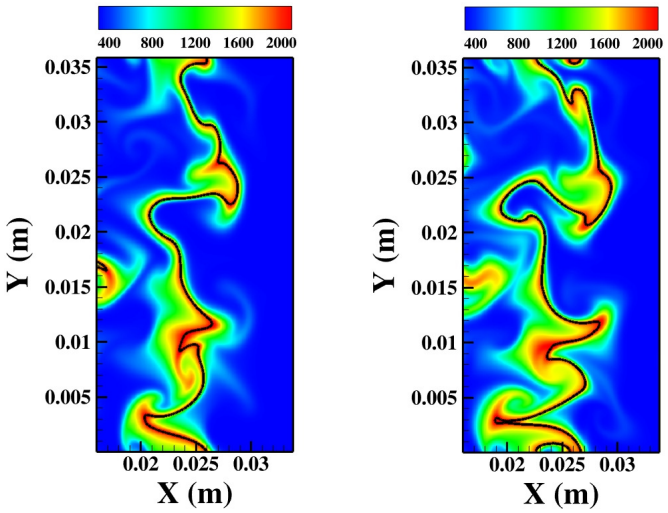


(c) $t = \tau$




(d) $t = 1.5\tau$

Figure 3.8: Contour plots of temperature (in K) for the inverse flame (stoichiometric mixture fraction ($Z_{st} = 0.056$) plotted as a black line).

configuration is more efficient at oxidizing the precursor.

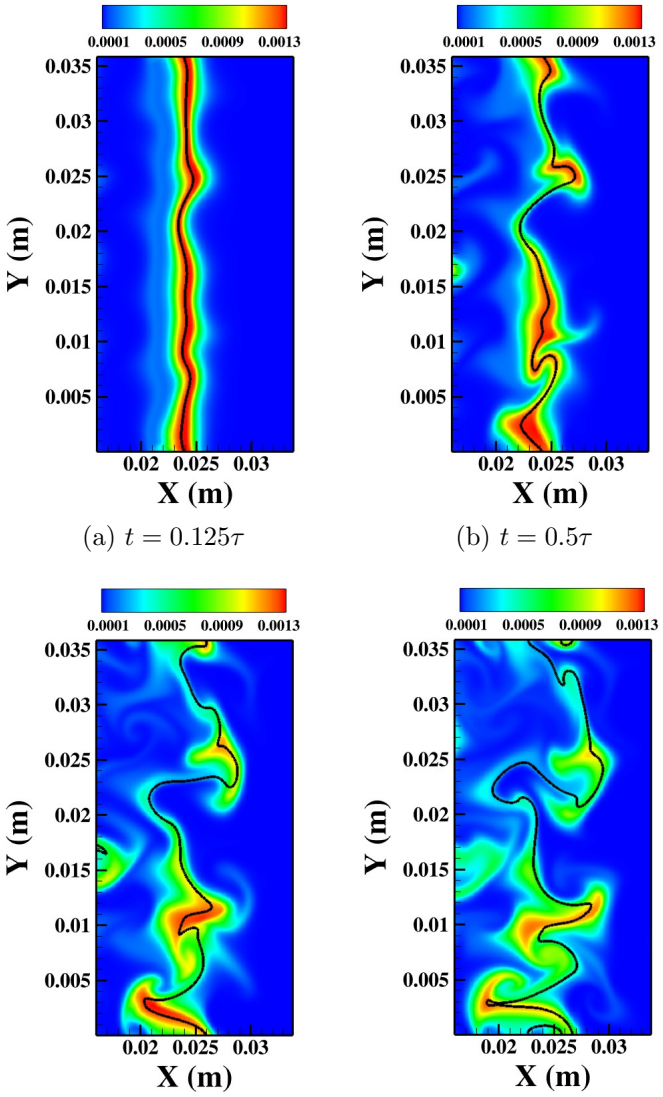


(a) $t = 0.125\tau$ (b) $t = 0.5\tau$

(c) $t = \tau$ (d) $t = 1.5\tau$

Figure 3.9: Contour plots of mass fraction of $TiO_2$ for the inverse flame (stoichiometric mixture fraction ($Z_{st} = 0.056$) plotted as a black line).

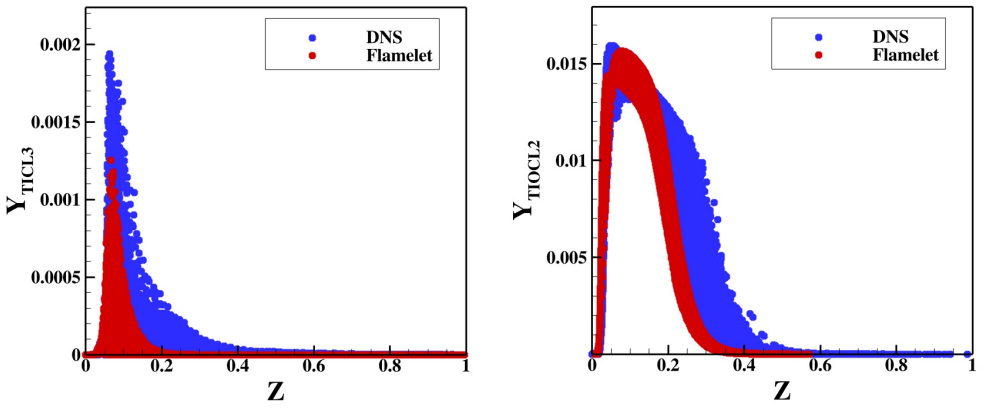


(a) $TiCl_3$




(b) $TiOCl_2$

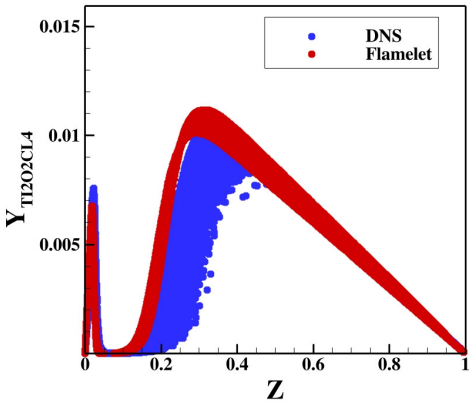


(c) $Ti_2O_2Cl_4$

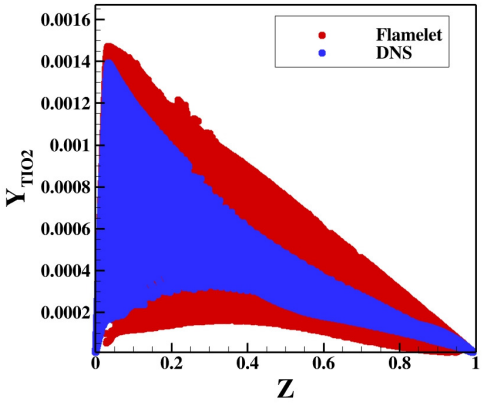


(d) $TiO_2$

Figure 3.10: Comparison of flamelet and DNS values for the inverse flame at $t = \tau$.

Conditional scatter plots of monomer ($TiOCl_2$) and dimer species ($TiO_2Cl_4$) shown in Figures 3.10b and 3.10c indicate that the formation of these species proceeds similar to the normal flame configuration. This provides further ev-

idence that the reactions leading to these species are slower compared to the flame chemistry. In spite of the availability of excess oxygen, turbulent convection and diffusion are able to move the mixture into the fuel-rich side before oxidation is completed.

# Chapter 4

# Reaction Path Analysis of 46 Species Mechanism

## 4.1 Motivation

For the DNS simulations, a quantity of particular interest was the distribution of the source term for $TiO_2$ ($\dot{\omega}_{TiO_2}$ from equation 2.3) as a function of mixture fraction. The distribution would show where in the flame that titania was being formed. Figure 4.1 shows a conditional plot of the $TiO_2$ source term versus mixture fraction at $t = \tau$. From Figure 4.1, it is clear that $\dot{\omega}_{TiO_2}$ has

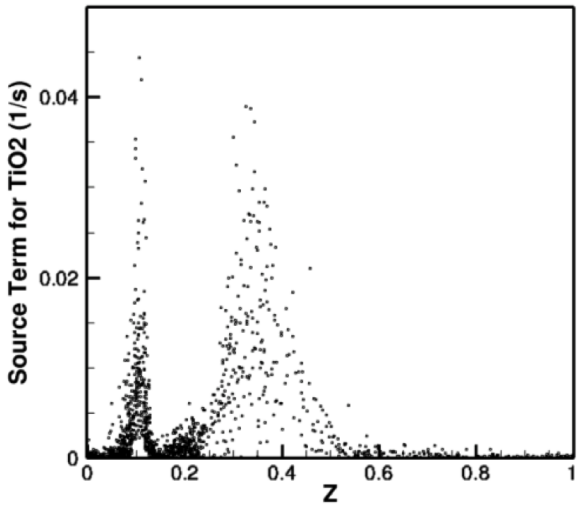


Figure 4.1: $TiO_2$ source terms vs. mixture fraction

two peak values, one on the lean side around $Z \approx 0.1$ and one on the rich side near $Z \approx 0.35$. Different reaction pathways are dominant at different mixture fractions. This indicates that $TiO_2$ can be formed via different pathways.

## 4.2 Reaction Path Analysis

To identify and gain a better understanding of these pathways, a reaction flow analysis was performed using the FlameMaster code [36]. An unstretched premix flame was simulated in 1-D with initial mass fractions adapted from the nonpremixed flames from the study by Pratsinis [6]. For the nonpremixed flame (Flame D configuration), the mass fractions for the fuel are given below.

$$Y_{Ar} = 0.555$$

$$Y_{CH_4} = 0.278$$

$$Y_{TiCl_4} = 0.167$$

The corresponding mass fractions for the oxidizer side are listed below.

$$Y_{O_2} = 0.233$$

$$Y_{N_2} = 0.767$$

For the unburnt side boundary conditions of the premixed flame, it was assumed that the fuel side and oxidizer side each kept their respective mass fraction ratios. For example, the ratio of $Y_{Ar}$ to $Y_{CH_4}$ was kept at $\frac{0.555}{0.278}$ with the amount of fuel relative to oxidizer changing based on the equivalence ratio. However, the FlameMaster code calculates the equivalence ratio of the

unburnt mixture based solely on the amount of $CH_4$ versus $O_2$ and does not take into account any of the inert species.

$$\phi = \frac{m_{ox}/m_{fuel}}{(m_{ox}/m_{fuel})st} \tag{4.1}$$

where the stoichiometric ratio of oxidizer to fuel is calculated based on the global reaction given by equation 4.2.

$$TiCl_4 + CH_4 + 3O_2 \rightarrow TiO_2 + 2H_2O + CO_2 + Cl_2 \tag{4.2}$$

FlameMaster calculates the mixture fraction by using the equations 4.3 and 4.5.

$$Z_{st} = \frac{1}{1+\Phi} \tag{4.3}$$

where $\Phi$ is given by equation 4.4

$$\Phi = \frac{\nu_O MW_O Y_{F,0}}{\nu_F MW_F Y_{O,0}} \tag{4.4}$$

where $\nu$ is the stoichiometric coefficient in the global equation, $MW$ is the molecular weight, $Y_{F,0}$ is the mass fraction of $CH_4$ in the fuel, and $Y_{O,0}$ is the mass fraction of $O_2$ in air.

$$\phi = \frac{Z}{1-Z}\frac{1-Z_{st}}{Z_{st}} \tag{4.5}$$

where $Z$ can be back-calculated from equation 4.5. $Z_{st}$ was calculated to be 0.122. However, the actual stoichiometric mixture fraction was higher because the FlameMaster code did not account for the other species in the fuel. Instead, $Z_{st}$ was found by locating the mixture fraction at which temperature was at

a maximum. This corresponded to $Z \approx 0.17$ which is consistent with the nonpremixed case.

Next, the premixed flame simulation was run for mixture fraction values ranging from 0.100 to 0.208. The range was limited due to the flammability limits of the premixed flame. Figure 4.2 shows maximum temperature and the temperature 10 mm away from the unburnt gas boundary versus mixture fraction for the premixed flame. The burning velocity of the flame is shown

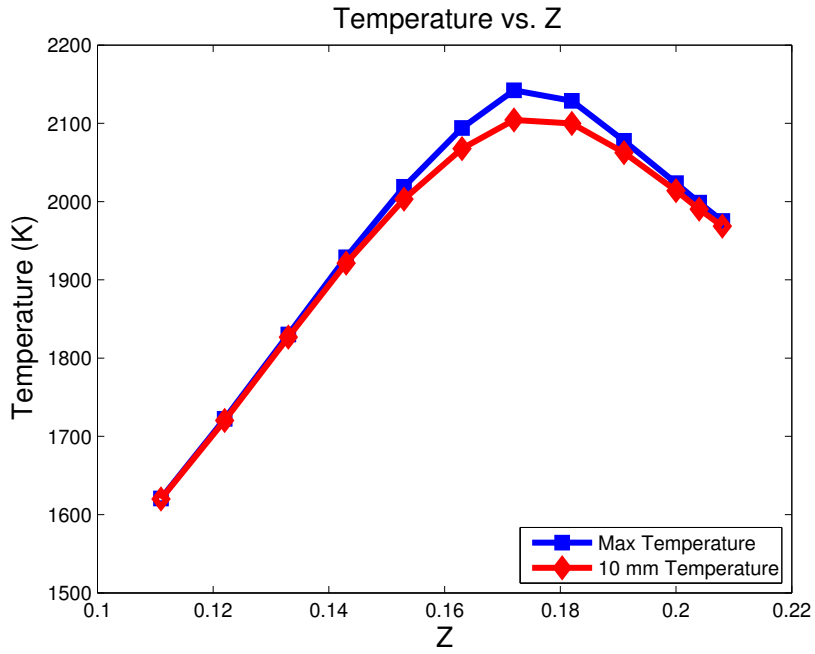


Figure 4.2: Temperature vs. mixture fraction

in Figure 4.3. From these two figures, it can be seen that the burning velocity peaks just rich of the stoichiometric mixture fraction value, and that the separation between the maximum temperature and the 10 mm temperature is the

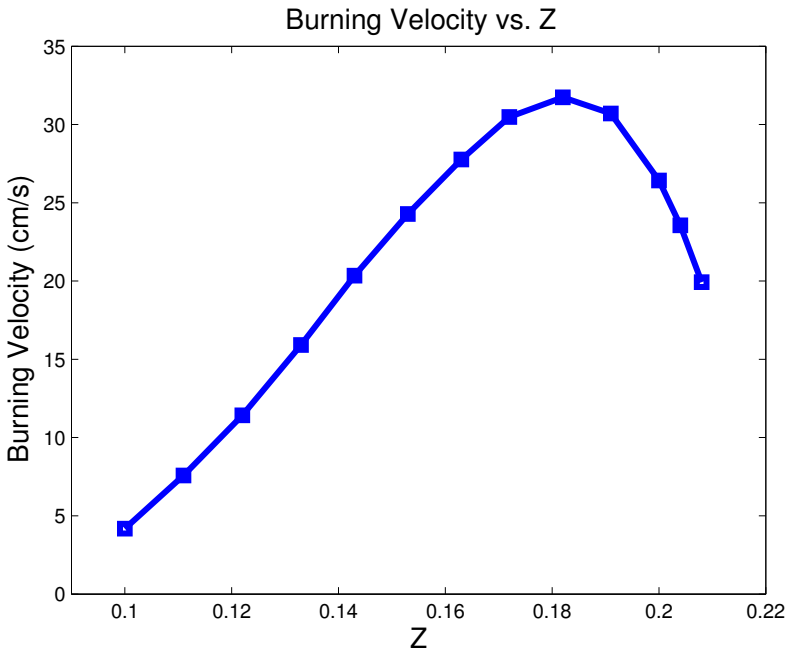


Figure 4.3: Burning velocity (cm/s) vs. mixture fraction

greatest where the burning velocity is the highest and the flame is thinnest.

Next, the integral reaction flow analysis was performed, by calculating the overall production or consumption of species during each reaction.For the 1-D premixed flame, the integration is spatial over the reaction zone and given by equation 4.6.

$$PR_{i,j} = \sum_{k=1}^{m} -\nu_{i,j} RR_j \frac{x_{k+1} - x_{k-1}}{2} MW_i \tag{4.6}$$

where $i$ is the species index, $j$ is the reaction index, $k$ is the grid index, $m$ is the number of grid points, $\nu$ is the difference between the stoichiometric coefficients of the products and reactants of the $i$th species, $MW$ is the molecular weight

of each species, and $RR$ is the overall reaction rate given by the difference between the forward and backward reaction rates.

$$RR = RR_{forward} - RR_{backward} \tag{4.7}$$

Next, the production rates were added together for each species.

$$PR_i = \sum_{j=1}^{n} PR_{i,j} \tag{4.8}$$

where $n$ is the total number of reactions. In addition to the absolute rates of production being calculated, the relative rates are calculated as well by taking the the ratio of the rate of production of species $i$ for reaction $j$ to the sum of the rates of production of species $i$ for all $n$ reactions.

$$PR_{rel_{i,j}} = \frac{PR_{i,j}}{PR_i} \tag{4.9}$$

The relative production rates are generally expressed in terms of percent. The reaction pathways with the largest relative production rates are the most important pathways. According to Warnatz, if the relative production rate of a reaction is less than 1% for the range of mixture fractions, then it is unimportant and can be disregarded [37].

The reaction process for titania nanoparticle nucleation begins with $TiCl_4$. Looking at the relative production rates, it was found that $TiCl_4$ is consumed primarily by two reactions (280f and 286f), to form $TiCl_3$.

$$TiCl_4 + M \rightarrow TiCl_3 + Cl + M \tag{280f}$$

$$TiCl_4 + Cl \rightarrow TiCl_3 + Cl_2 \tag{286f}$$

Figure 4.4 shows the relative production rates of $TiCl_4$. The negative values indicate that $TiCl_4$ is being consumed. As the mixture fraction increases,

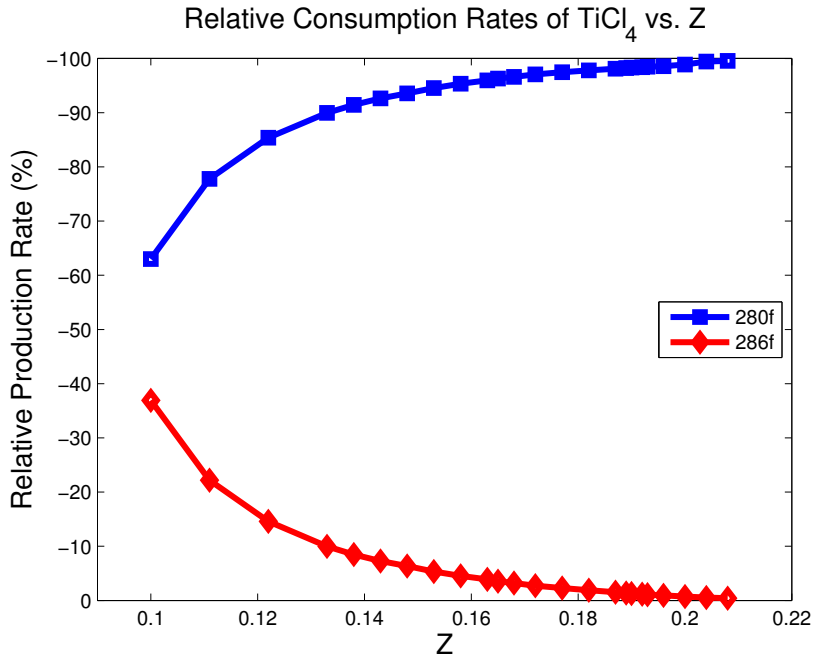


Figure 4.4: Relative consumption rate (%) of $TiCl_4$ vs. mixture fraction

reaction 280f becomes more dominant. Using either reaction though, $TiCl_3$ is the product. Not surprisingly, $TiCl_3$ forms mainly from those two reactions as shown in Figure 4.5. Next, $TiCl_3$ is consumed by several different reactions that are dominant at different mixture fractions as seen in Figure 4.6. This is where the lean and rich paths diverge and will be addressed separately.

At low mixture fraction values, Figure 4.6 indicates that reactions 311f and 298f are comparable in terms of consumption rates and form the products

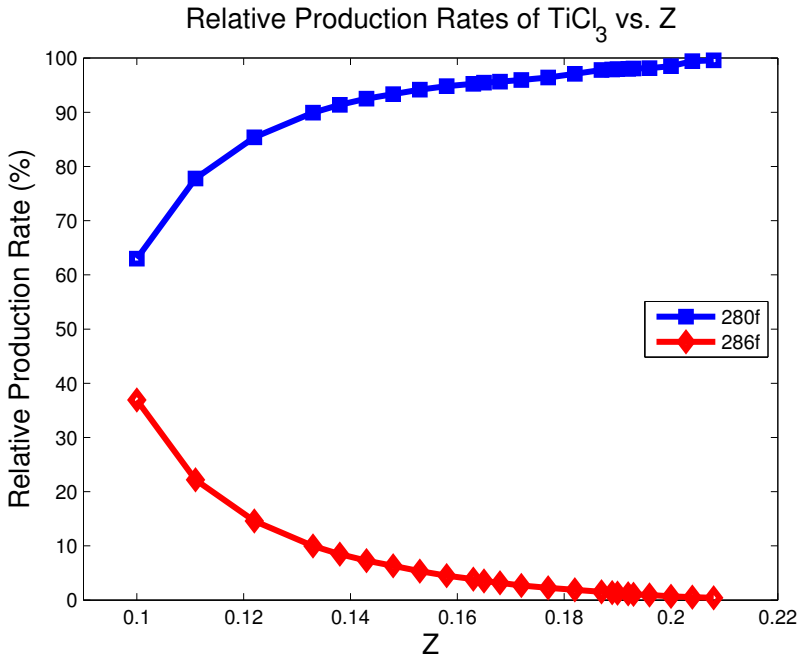


Figure 4.5: Relative production rate (%) of $TiCl_3$ vs. mixture fraction

$TiOCl_2$ and $TiO_2Cl_3$ respectively.

$$TiCl_3 + O \rightarrow TiOCl_2 + Cl \tag{311f}$$

$$TiCl_3 + O_2 + M \rightarrow TiO_2Cl_3 + M \tag{298f}$$

First, looking at $TiO_2Cl_3$, it is formed almost exclusively from reaction $298f$. Its relative consumption rates are shown in Figure 4.7. At lean Z values, reaction 330f is dominant and forms $Ti_2O_2Cl_6$.

$$TiO_2Cl_3 + TiCl_3 \rightarrow Ti_2O_2Cl_6 \tag{330f}$$

Next, $Ti_2O_2Cl_6$ is consumed solely by the dissociation reaction 331f into $TiOCl_3$.

$$Ti_2O_2Cl_6 \rightarrow 2TiOCl_3 \tag{331f}$$

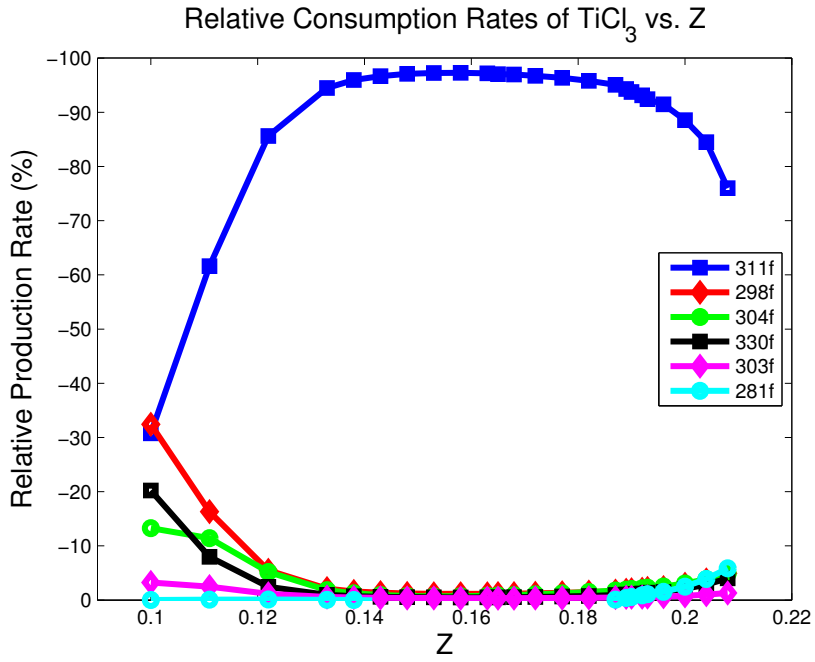


Figure 4.6: Relative consumption rate (%) of $TiCl_3$ vs. mixture fraction

Moving along, the relative production rates for $TiOCl_3$ are shown in Figure 4.8. For low mixture fraction values, reaction 331f is clearly the most important reaction. Next $TiOCl_3$ is consumed almost exclusively (relative consumption rates at 99.9%) by reaction 300f to form $TiOCl_2$ which is also one of the main products of the reaction 311f.

$$TiOCl_3 \rightarrow TiOCl_2 + Cl \qquad (300f)$$

Next, the relative production rates of $TiOCl_2$ are shown in Figure 4.9. The two reactions that are dominant are 300f and 311f. Whether or not the direct pathway (311f) is taken, both paths lead to the formation of $TiOCl_2$. Next,

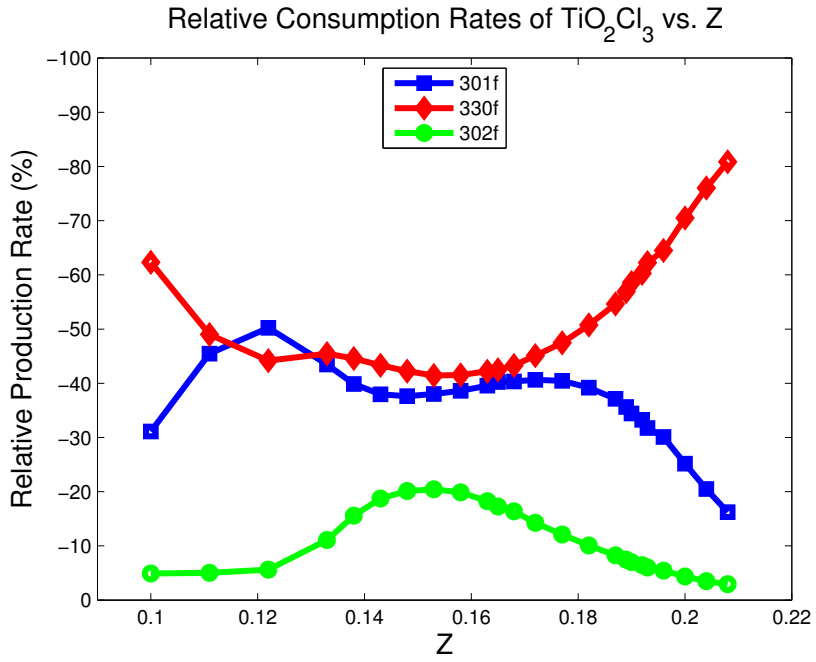


Figure 4.7: Relative consumption rate (%) of $TiO_2Cl_3$ vs. mixture fraction

the relative consumption rates are shown in Figure 4.10. At low Z values, reaction 323f is the most important, but reactions 325f and 327f turn out to be significant as well.

$$2TiOCl_2 \rightarrow Ti_2O_2Cl_4 \tag{323f}$$

$$TiOCl_2 + TiO_2Cl_2 \rightarrow Ti_2O_3Cl_3 + Cl \tag{325f}$$

$$TiOCl_2 + Ti_2O_3Cl_3 \rightarrow Ti_3O_4Cl_4 + Cl \tag{327f}$$

To explain why those two reactions are important, one must move backwards from the final product. $TiO_2$ is formed in reaction 349 by $Ti_5O_6Cl_8$. Before

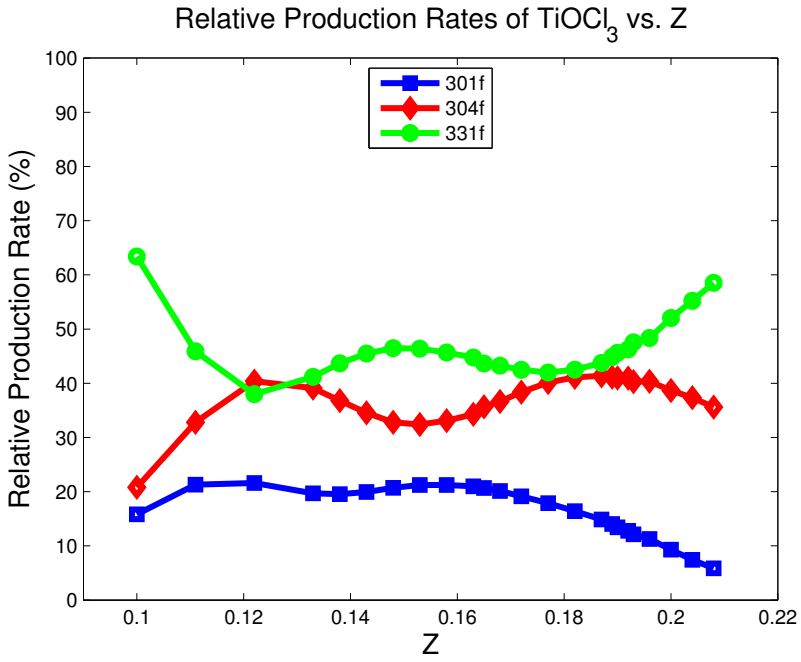


Figure 4.8: Relative production rate (%) of $TiOCl_3$ vs. mixture fraction

that, $Ti_5O_6Cl_8$ must be produced via reaction 346.

$$Ti_5O_6Cl_8 + 2O_2 \rightarrow 5TiO_2 + 4Cl_2 \tag{349}$$

$$Ti_2O_2Cl_4 + Ti_3O_4Cl_4 \rightarrow Ti_5O_6Cl_8 \tag{346}$$

As evident from reaction 346, both $Ti_2O_2Cl_4$ and $Ti_3O_4Cl_4$ must be present. Reaction 325f followed by reaction 327f is responsible for the formation of $Ti_3O_4Cl_4$.

The relative production and consumption rates for $Ti_2O_2Cl_4$ versus mixture fraction are shown in Figure 4.11. Both are shown in the same figure because some reactions change directions depending on the mixture fraction

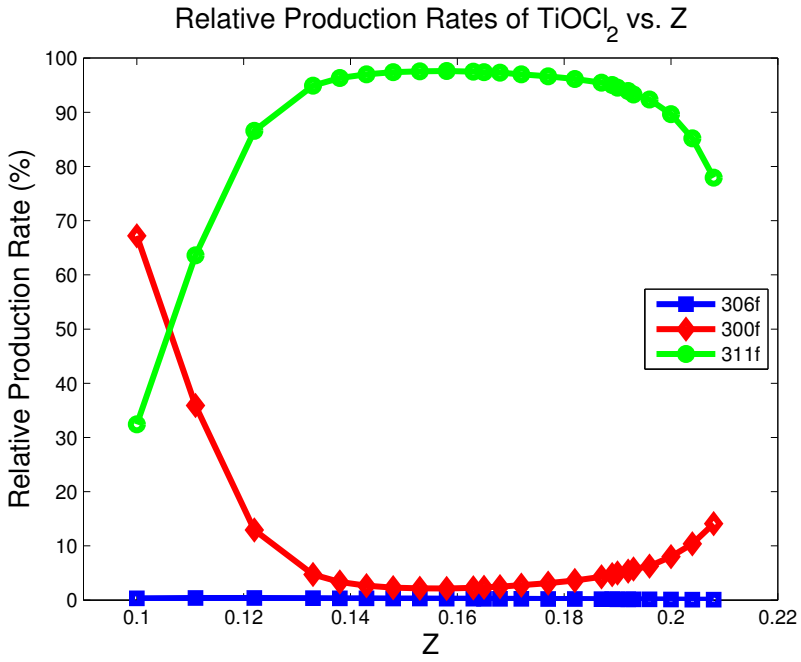


Figure 4.9: Relative production rate (%) of $TiOCl_2$ vs. mixture fraction

values. For the lean pathway, reaction 323f is the main production reaction and 346 is the main consumption reaction. Reactions 346 and 349 complete the lean pathway. The full dominant path is shown in Figure 4.12. To see how successful the lean pathway is at producing titania, the absolute production rates are the desired metric. Starting with $TiO_2$ and working backwards, it is apparent that the integrated production rate reaches a maximum at a lean mixture fraction value of $Z \approx 0.11$. This is comparable to what the DNS data suggests. On the rich side of Figure 4.13, the production rate appears to be reaching another maximum value. Unfortunately, the flammability limits of the premixed flame prevent do not allow a solution to be converged upon at

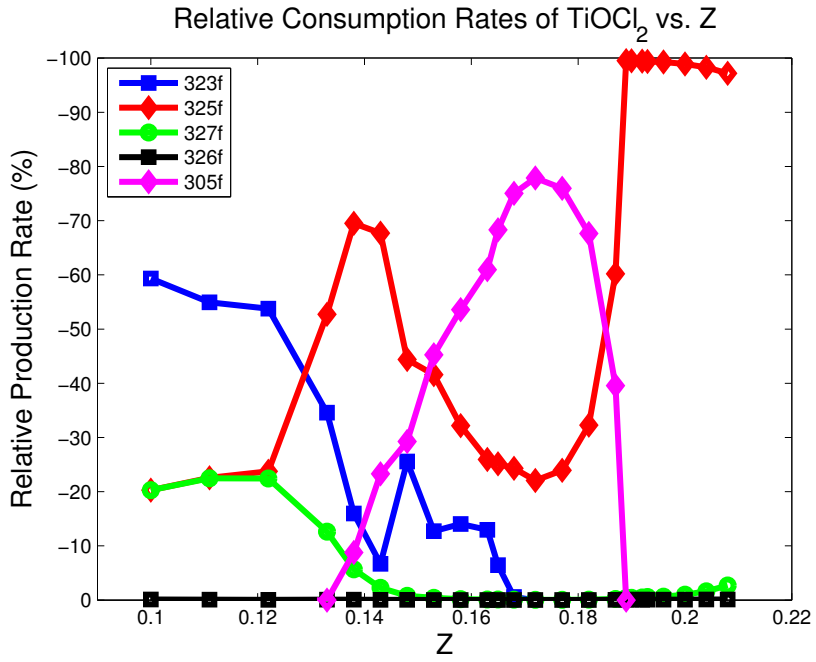


Figure 4.10: Relative consumption rate (%) of $TiOCl_2$ vs. mixture fraction

higher equivalence ratios. For $Ti_5O_6Cl_8$ and $Ti_3O_4Cl_4$, the distributions of the integrated production rates are the same shape as in Figure 4.13 for $TiO_2$. The integrated production rates for the reactions forming $Ti_2O_2Cl_4$ are shown in Figure 4.16. Figure 4.16 also indicates that a maximum production rate is reached on the lean side with values then decreasing and finally increasing again as the mixture becomes more rich. Next, the rich pathway was analyzed using the same technique.

For high Z values, the pathway is noticeably different than for low Z values. Starting with $TiCl_3$, Figure 4.6 shows that reaction 311f is clearly

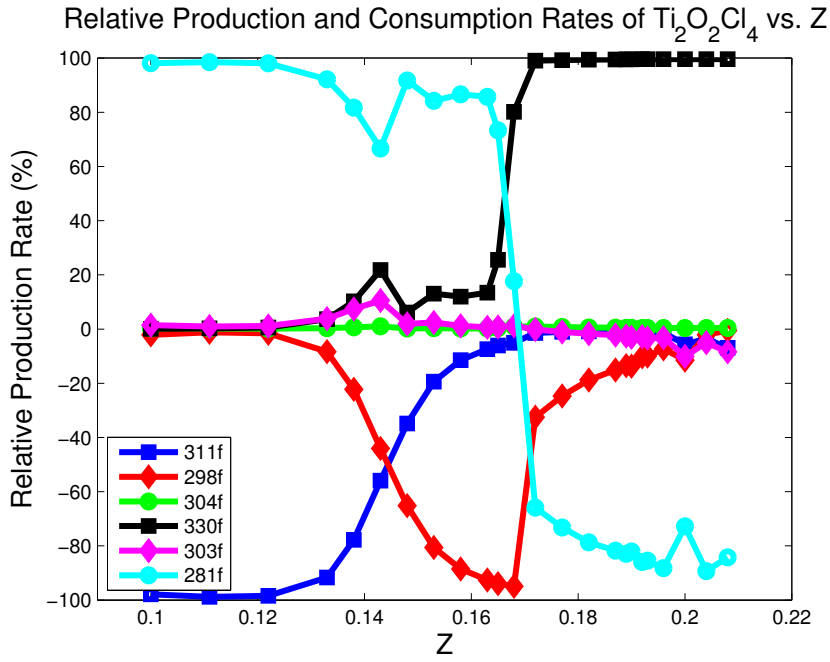


Figure 4.11: Relative production rate (%) of $Ti_2O_2Cl_4$ vs. mixture fraction

dominant. However, reactions 303f and 324f prove to be important as well.

$$TiCl_3 + O_2 \rightarrow TiO_2Cl_2 + Cl \tag{303f}$$

$$TiCl_3 + TiO_2Cl_2 \rightarrow Ti_2O_2Cl_4 + Cl \tag{324f}$$

Reaction 303f forms $TiO_2Cl_2$ which is used in reaction 324f along with $TiCl_3$ to form $Ti_2O_2Cl_4$, which is one of the two important reactants in reaction 346. In fact, reaction 324 is the main reaction responsible for production of $Ti_2O_2Cl_4$. For the lean pathway, reaction 323f formed $Ti_2O_2Cl_4$, but on the rich side, this reaction proceeds in the opposite direction and dissociation into $TiOCl_2$ occurs instead. This trend is illustrated in Figure 4.11. Again, like in

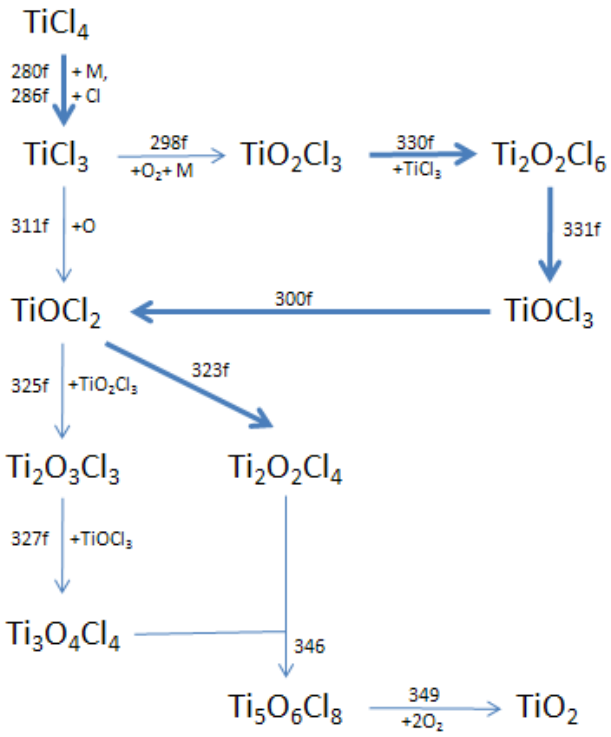


Figure 4.12: Lean reaction pathway

the lean case, there are two paths from $TiCl_3$ and both lead to the formation of $TiOCl_2$. Looking at the consumption of $TiOCl_2$ in Figure 4.10, it is clear that reaction 325f is dominant. Next, $Ti_2O_3Cl_3$ is converted into $Ti_3O_4Cl_4$ via reaction 327f. Then, like the lean pathway, reactions 346 and 349 are then undergone to form $TiO_2$. The full diagram of the rich pathway is shown in Figure 4.17.

Lastly. the pathway for near-stoichiometric mixture fraction values was analyzed in order to see why $TiO_2$ was being produced in smaller amounts

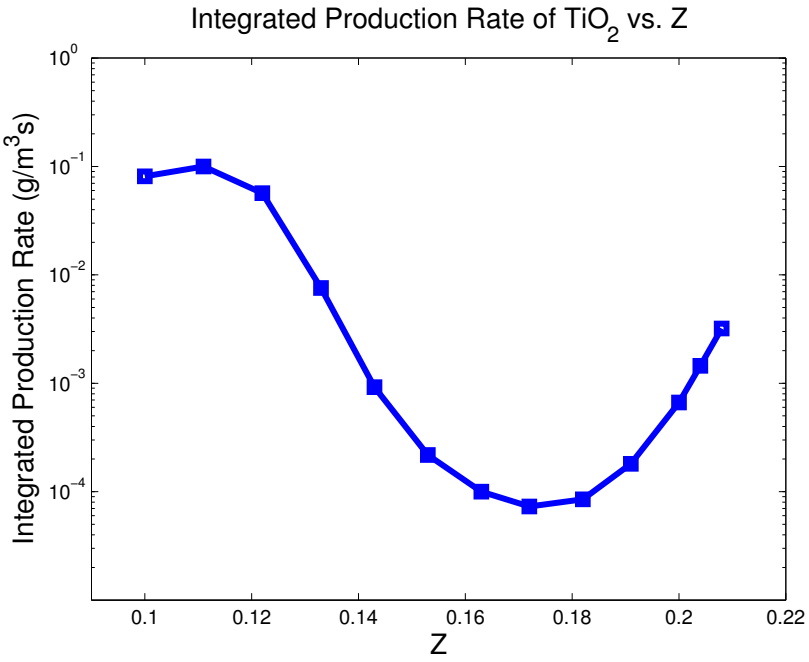


Figure 4.13: Integrated production rate (log scale) of $TiO_2$ vs. mixture fraction

for this mixture. Although the path shares some characteristics with the rich pathway, there are a few notable differences. First, the dominant consumption reaction of $TiOCl_2$ is reaction 305f (as seen in Figure 4.10) which forms $TiCl_2$ which in turn forms $TiCl_3$ via reactions 296f and 281f. The increase in the relative production rate of reaction 305f probably results from an increase in the formation O radicals at high temperatures near $Z_{st}$.

$$TiOCl_2 + O \rightarrow TiCl_2 + O_2 \tag{305f}$$

$$TiCl_2 + TiCl_4 \rightarrow 2TiCl_3 \tag{296f}$$

$$TiCl_2 + Cl + M \rightarrow TiCl_3 + M \tag{281f}$$

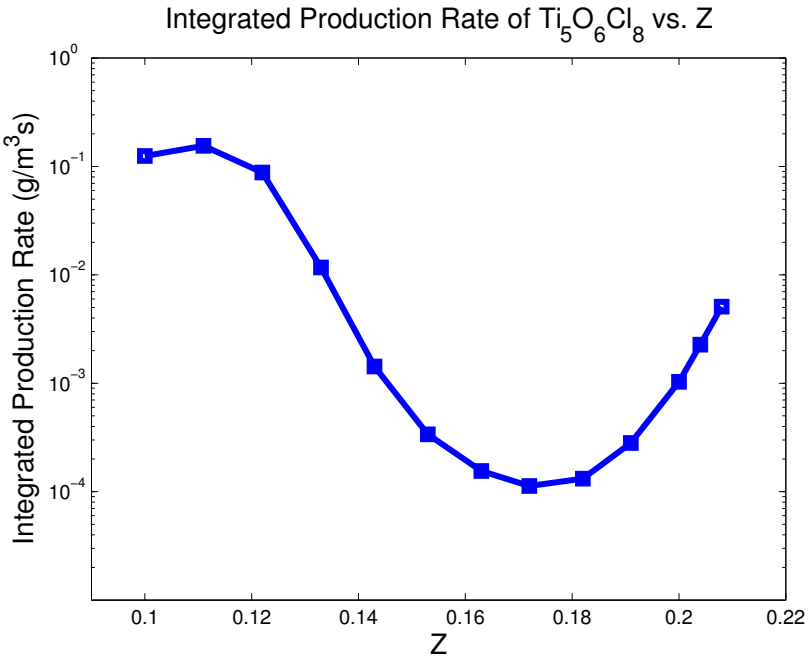


Figure 4.14: Integrated production rate (log scale) of $Ti_5O_6Cl_8$ vs. mixture fraction

Essentially, the reaction path is going back upstream in the process to an earlier species. Later in the process, reaction 327f which forms $Ti_3O_4Cl_4$ has to compete with reaction 328f which forms the stable intermediate $Ti_2O_3Cl_2$.

$$Ti_2O_3Cl_3 \rightarrow Ti_2O_3Cl_2 + Cl \tag{328f}$$

At near-stoichiometric Z values, reaction 328f is dominant thereby limiting the production of $Ti_3O_4Cl_4$. Because of the formation of stable intermediates and the reaction pathway returning from $TiOCl_2$ to $TiCl_3$, the production of $TiO_2$ is limited at near-stoichiometric mixture fractions. The diagram of the near-stoichiometric pathway is shown in Figure 4.18.

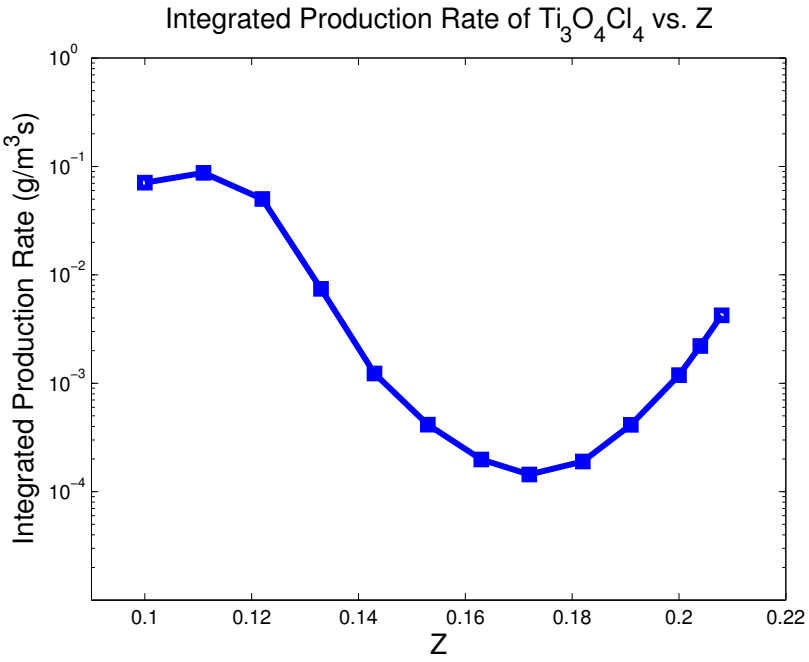


Figure 4.15: Integrated production rate (log scale) of $Ti_3O_4Cl_4$ vs. mixture fraction

After looking at each pathway, reaction 347 was noted to be completely insignificant for all mixture fraction values tested.

$$Ti_2O_2Cl_6 + Ti_3O_4Cl_4 \rightarrow Ti_5O_6Cl_8 + Cl_2 \tag{347}$$

Instead, $Ti_2O_2Cl_6$ was dissociated via reaction 331f to form $TiOCl_3$. By the criteria set by Warnatz, this reaction can be eliminated from the mechanism [37]. Another reaction that can be eliminated is 287f.

$$TiCl_3 + Cl \rightarrow TiCl_2 + Cl_2 \tag{287f}$$

The transition from $TiCl_3$ to $TiCl_2$ and vice versa is dominated by reactions

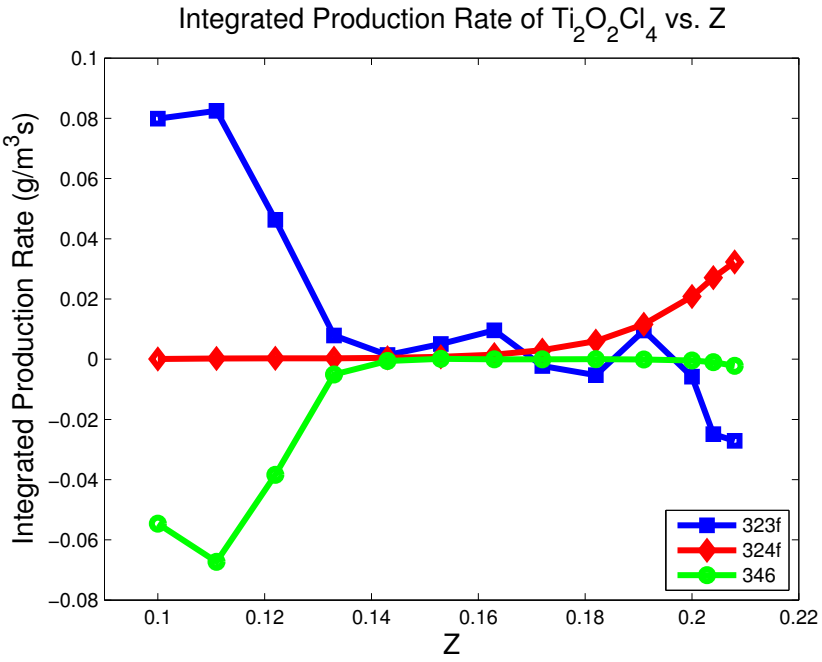


Figure 4.16: Integrated production rate of $Ti_2O_2Cl_4$ vs. mixture fraction

296f and 281f. Reaction 326f can also be eliminated as reactions 323f and 324f have much higher production rates of $Ti_2O_2Cl_4$.

$$TiOCl_2 + TiOCl_3 \rightarrow Ti_2O_2Cl_4 + Cl \tag{326f}$$

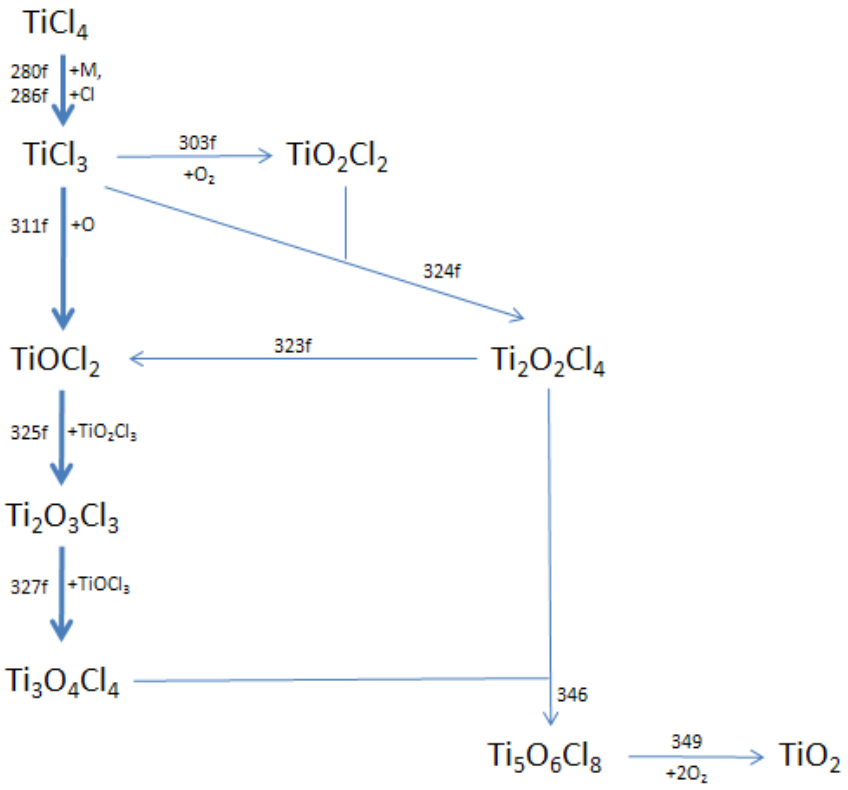


Figure 4.17: Rich reaction pathway

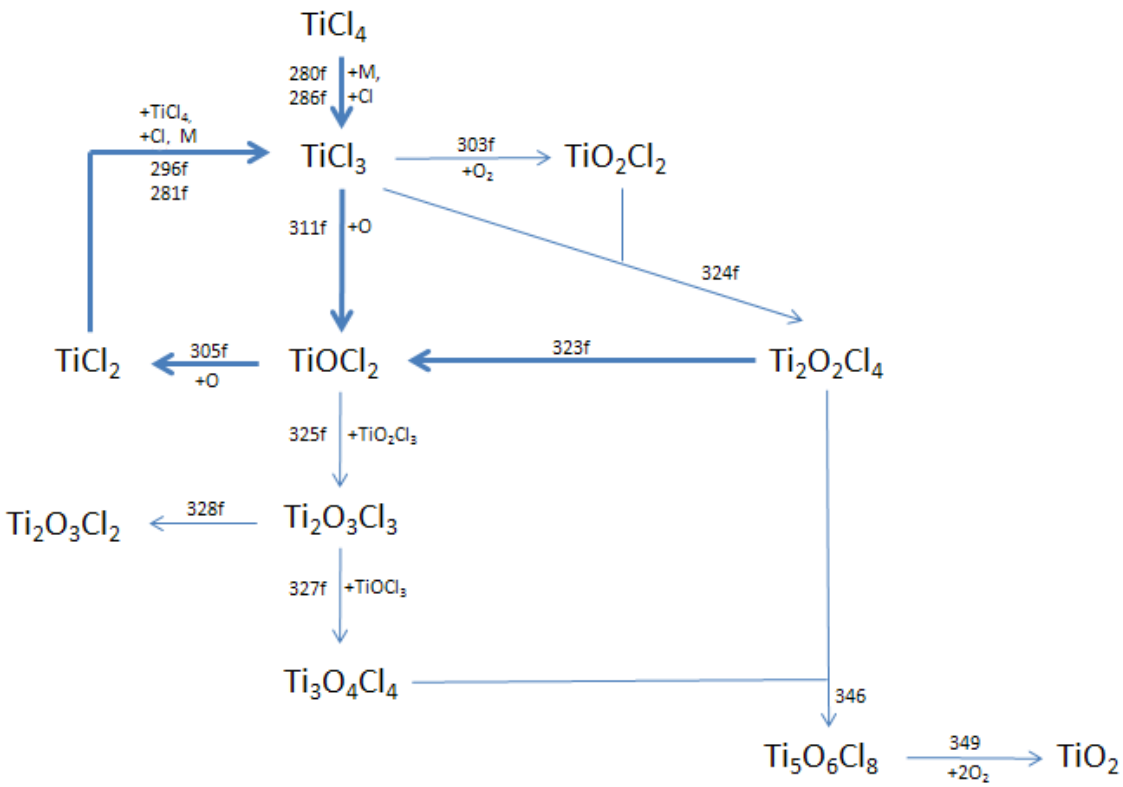


Figure 4.18: Near-stoichiometric reaction pathway

# Chapter 5

# Conclusions and Future Works

## 5.1 Conclusions

The DNS studies have provided a comprehensive view of the precursor oxidation structure in methane/air flames based on a multi-step chemical mechanism. Based on this mechanism, the flame configuration appears to have limited effect on the conversion efficiency of the precursor. Although the inverse flame was expected to be more efficient due to the direct access to excess oxygen, precursor oxidation was still limited by the formation rates of monomer and dimer species. Consequently, both the normal and inverse flames provided relatively small conversion rate to titania. This effect arises from the temperature insensitivity of certain key reactions in the pathway, which reduces the reaction rates as compared to the hydrocarbon chemistry. In general, oxidation of the Ti-species occurs over time scales comparable to convective transport.

The DNS study also compared the DNS results to a one-dimensional laminar flamelet solution. It was found that titania formation and hydrocarbon species were generally well predicted by the flamelet model. If the precursor mass fraction in the fuel/oxidizer streams increases, it is likely that

increased competition for oxygen will render the flamelet model inaccurate for hydrocarbon species. However, the overall structure of precursor oxidation, especially the delayed formation of $TiO_2Cl_4$ is captured by the flamelet model.

During the analysis of the DNS results, it was found that the source term had a bimodal distribution in relation to mixture fraction. This indicated that titania was formed on the lean and rich sides of the flame and that there were different chemical reaction pathways followed depending on the mixture. A reaction path analysis was performed and confirmed that fuel-lean and fuel-rich mixtures led to different pathways being followed to reach $TiO_2$. Optimal mixture fraction values were found that maximized the conversion of $TiCl_4$ to $TiO_2$.

## 5.2 Future Works

It is important to note that these conclusions are driven primarily by the chemistry mechanism. Although the initial decomposition reactions of the precursor have been well characterized, many of the critical reactions in the formation of the oxidized Ti-species have been treated as barrier-less reactions due to the lack of additional data. The study by Totton et al. [22] produced thermodynamic data for all important species in the flame synthesis process. The next step is to develop the reaction mechanism for this system. Once reactions with accurate reaction rates are found, the conclusions of this study should be revisited.

Also, the DNS study only modeled the nucleation of the titania nanopar-

ticles. Currently, the author is working on adding nanoparticle evolution processes (aggregation, growth, and sintering) to the DNS code by adding a population balance model that utilizes conditioned quadrature method of moments (CQMOM). This will give insight into how nanoparticle characteristics are affected by turbulent transport in the flame.

# Appendices

# Appendix A

# 46 Species Mechanism

| No | Reaction | $A_n$ | $b_n$ | $E_n$ |
|---|---|---|---|---|
| 1 | $TiCL_4$+M $\rightleftharpoons$ $TiCL_3$+CL+M | 5.400E+18 | 0.000 | 80236.850 |
| 2 | $TiCL_3$+$CL_2$ $\rightleftharpoons$ $TiCL_4$+CL | 1.000E+13 | 0.000 | 0.000 |
| 3 | 2$TiCL_3$ $\rightleftharpoons$ $TiCL_2$+$TiCL_4$ | 9.600E+12 | 0.000 | 8358.030 |
| 4 | $TiCL_3$+M$\rightleftharpoons$ $TiCL_2$+CL+M | 7.700E+18 | 0.000 | 92415.630 |
| 5 | 2CL+M$\rightleftharpoons$ $CL_2$+M | 2.230E+14 | 0.000 | -1798.280 |
| 6 | $TiCL_2$+$CL_2$$\rightleftharpoons$ $TiCL_4$ | 1.000E+13 | 0.000 | 0.000 |
| 7 | $TiCL_2$+$CL_2$$\rightleftharpoons$ $TiCL_3$+CL | 1.000E+13 | 0.000 | 0.000 |
| 8 | 2H+M$\rightleftharpoons$ $H_2$+M | 1.000E+18 | -1.000 | 0.000 |
| | third-body efficiencies / AR 0.6 / $H_2$ 0.0 / $H_2O$ 0.0 / $CH_4$ 2.0 / $C_2H_6$ 3.0 / $CO_2$ 0.0 / | | | |
| 9 | 2H+$H_2$$\rightleftharpoons$ 2$H_2$ | 9.000E+16 | -0.600 | 0.000 |
| 10 | $TiCL_3$+O$\rightleftharpoons$ $TiOCL_2$+CL | 1.000E+13 | 0.000 | 0.000 |
| 11 | 2O+M$\rightleftharpoons$ $O_2$+M | 1.200E+17 | -1.000 | 0.000 |
| | third-body efficiencies / AR 0.8 / $H_2$ 2.4 / $H_2O$ 15.4 / $CH_4$ 2.0 / $C_2H_6$ 3.0 / CO 1.8 / $CO_2$ 3.6 / | | | |
| 12 | O+$H_2$$\rightleftharpoons$ H+OH | 5.000E+04 | 2.670 | 6289.910 |
| 13 | O+H+M$\rightleftharpoons$ OH+M | 5.000E+17 | -1.000 | 0.000 |
| | third-body efficiencies / AR 0.7 / $H_2$ 2.0 / $H_2O$ 6.0 / $CH_4$ 2.0 / $C_2H_6$ 3.0 / CO 1.5 / $CO_2$ 2.0 / | | | |
| 14 | $TiOCL_2$+$TiOCL_3$$\rightleftharpoons$ $Ti2O_2CL_4$+CL | 1.000E+13 | 0.000 | 0.000 |
| 15 | 2$TiOCL_3$$\rightleftharpoons$ $Ti2O_2CL_6$ | 1.000E+13 | 0.000 | 0.000 |
| 16 | $TiOCL_3$+O$\rightleftharpoons$ $TiCL_3$+$O_2$ | 1.000E+13 | 0.000 | 0.000 |
| 17 | $TiOCL_3$+O$\rightleftharpoons$ $TiO_2CL_3$ | 1.000E+13 | 0.000 | 0.000 |
| 18 | $TiOCL_2$+CL$\rightleftharpoons$ $TiOCL_3$ | 1.000E+13 | 0.000 | 0.000 |
| 19 | 2$TiOCL_2$$\rightleftharpoons$ $Ti2O_2CL_4$ | 1.000E+13 | 0.000 | 0.000 |
| 20 | OH+$H_2$$\rightleftharpoons$ H+$H_2O$ | 2.160E+08 | 1.510 | 3429.970 |
| 21 | H+OH+M$\rightleftharpoons$ $H_2O$+M | 2.200E+22 | -2.000 | 0.000 |
| | third-body efficiencies / AR 0.4 / $H_2$ 0.7 / $H_2O$ 3.6 / $CH_4$ 2.0 / $C_2H_6$ 3.0 / | | | |

| No | Reaction | | $A_n$ | $b_n$ | $E_n$ |
|---|---|---|---|---|---|
| 22 | $2OH \rightleftharpoons O+H_2O$ | | 3.570E+04 | 2.400 | -2109.940 |
| 23 | $2OH(+M) \rightleftharpoons H_2O_2(+M)$ | $k_\infty$ | 7.400E+13 | -0.370 | 0.000 |
| | | $k_0$ | 2.30E+18 | -0.90 | -1700.0 |
| | $a_0 = 0.8422$ $a_1 = 125$ $a_2 = 2219$ $a_3 = 6882$ | | | | |
| | third-body efficiencies / AR 0.7 / $H_2$ 2.0 / $H_2O$ 6.0 / $CH_4$ 2.0 / $C_2H_6$ 3.0 / CO 1.5 / $CO_2$ 2.0 / | | | | |
| 24 | $2H+H_2O \rightleftharpoons H_2+H_2O$ | | 6.000E+19 | -1.250 | 0.000 |
| 25 | $H+O_2+H_2O \rightleftharpoons HO_2+H_2O$ | | 9.380E+18 | -0.760 | 0.000 |
| 26 | $TiCL_3+O_2(+M) \rightleftharpoons TiO_2CL_3(+M)$ | $k_\infty$ | 1.925E+35 | -6.577 | 9891.010 |
| | | $k_0$ | 1.06E+36 | -6.32 | 0.0 |
| | $a_0 = 0.8422$ $a_1 = 125$ $a_2 = 2219$ $a_3 = 6882$ | | | | |
| 27 | $H+O_2+M \rightleftharpoons HO_2+M$ | | 2.800E+18 | -0.860 | 0.000 |
| | third-body efficiencies / $N_2$ 0.0 / AR 0.0 / $O_2$ 0.0 / $H_2O$ 0.0 / $C_2H_6$ 1.5 / CO 0.8 / $CO_2$ 1.5 / | | | | |
| 28 | $TiCL_2+O_2 \rightleftharpoons TiOCL_2+O$ | | 1.000E+13 | 0.000 | 0.000 |
| 29 | $H+2O_2 \rightleftharpoons HO_2+O_2$ | | 3.000E+20 | -1.720 | 0.000 |
| 30 | $H+O_2+AR \rightleftharpoons HO_2+AR$ | | 7.000E+17 | -0.800 | 0.000 |
| 31 | $H+O_2 \rightleftharpoons O+OH$ | | 8.300E+13 | 0.000 | 14413.000 |
| 32 | $TiO_2CL_2+TiOCL_2 \rightleftharpoons Ti2O_3CL_3+CL$ | | 1.000E+13 | 0.000 | 0.000 |
| 33 | $TiO_2CL_2+TiCL_3 \rightleftharpoons Ti2O_2CL_4+CL$ | | 1.000E+13 | 0.000 | 0.000 |
| 34 | $TiO_2CL_2+CL \rightleftharpoons TiCL_3+O_2$ | | 1.000E+13 | 0.000 | 0.000 |
| 35 | $TiO_2CL_2+CL \rightleftharpoons TiO_2CL_3$ | | 1.000E+13 | 0.000 | 0.000 |
| 36 | $TiO_2CL_2+O \rightleftharpoons TiOCL_2+O_2$ | | 1.000E+13 | 0.000 | 0.000 |
| 37 | $CL_2+TiO_2CL_2 \rightleftharpoons CL+TiO_2CL_3$ | | 1.000E+13 | 0.000 | 0.000 |
| 38 | $TiO_2CL_3+TiCL_3 \rightleftharpoons Ti2O_2CL_6$ | | 1.000E+13 | 0.000 | 0.000 |
| 39 | $CL_2+Ti2O_2CL_3 \rightleftharpoons CL+Ti2O_2CL_4$ | | 1.000E+13 | 0.000 | 0.000 |
| 40 | $Ti2O_2CL_3+TiCL_4 \rightleftharpoons Ti2O_2CL_4+TiCL_3$ | | 1.000E+13 | 0.000 | 0.000 |
| 41 | $H+HO_2 \rightleftharpoons O+H_2O$ | | 3.970E+12 | 0.000 | 670.890 |
| 42 | $H+HO_2 \rightleftharpoons 2OH$ | | 1.340E+14 | 0.000 | 635.040 |
| 43 | $2HO_2 \rightleftharpoons O_2+H_2O_2$ | | 1.300E+11 | 0.000 | -1630.020 |
| 44 | $H+HO_2 \rightleftharpoons O_2+H_2$ | | 2.800E+13 | 0.000 | 1068.120 |
| 45 | $2HO_2 \rightleftharpoons O_2+H_2O_2$ | | 4.200E+14 | 0.000 | 12000.000 |
| 46 | $OH+HO_2 \rightleftharpoons O_2+H_2O$ | | 2.900E+13 | 0.000 | -500.000 |

| No | Reaction | | $A_n$ | $b_n$ | $E_n$ |
|---|---|---|---|---|---|
| 47 | $O+HO_2 \rightleftharpoons OH+O_2$ | | 2.000E+13 | 0.000 | 0.000 |
| 48 | $O+H_2O_2 \rightleftharpoons OH+HO_2$ | | 9.630E+06 | 2.000 | 4000.000 |
| 49 | $OH+H_2O_2 \rightleftharpoons HO_2+H_2O$ | | 1.750E+12 | 0.000 | 320.030 |
| 50 | $H+H_2O_2 \rightleftharpoons HO_2+H_2$ | | 1.210E+07 | 2.000 | 5200.050 |
| 51 | $OH+H_2O_2 \rightleftharpoons HO_2+H_2O$ | | 5.800E+14 | 0.000 | 9559.990 |
| 52 | $H+H_2O_2 \rightleftharpoons OH+H_2O$ | | 1.000E+13 | 0.000 | 3599.900 |
| 53 | $Ti2O_3CL_3+TiOCL_2 \rightleftharpoons Ti3O_4CL_4+CL$ | | 1.000E+13 | 0.000 | 0.000 |
| 54 | $Ti2O_3CL_2+CL \rightleftharpoons Ti2O_3CL_3$ | | 1.000E+13 | 0.000 | 0.000 |
| 55 | $Ti2O_2CL_4+Ti3O_4CL_4 \rightleftharpoons Ti5O_6CL_8$ | | 1.000E+13 | 0.000 | 0.000 |
| 56 | $Ti2O_2CL_6+Ti3O_4CL_4 \rightleftharpoons Ti5O_6CL_8+CL_2$ | | 1.000E+13 | 0.000 | 0.000 |
| 57 | $Ti5O_6CL_8+2O_2 \rightleftharpoons 5TiO_2(ru)+4CL_2$ | | 1.000E+25 | 0.000 | 0.000 |
| 58 | $OH+CH_2 \rightleftharpoons H+CH_2O$ | | 2.000E+13 | 0.000 | 0.000 |
| 59 | $HO_2+CH_2 \rightleftharpoons OH+CH_2O$ | | 2.000E+13 | 0.000 | 0.000 |
| 60 | $CH_2+H_2 \rightleftharpoons H+CH_3$ | | 5.000E+05 | 2.000 | 7229.920 |
| 61 | $CH_2+O_2 \rightleftharpoons OH+HCO$ | | 1.320E+13 | 0.000 | 1500.000 |
| 62 | $O+CH_2 \rightleftharpoons H+HCO$ | | 8.000E+13 | 0.000 | 0.000 |
| 63 | $H+CH_2(+M) \rightleftharpoons CH_3(+M)$ | $k_\infty$ | 2.500E+16 | -0.800 | 0.000 |
| | | $k_0$ | 3.20E+27 | -3.14 | 1230.0 |
| | $a_0 = 0.8422$ $a_1 = 125$ $a_2 = 2219$ $a_3 = 6882$ | | | | |
| | third-body efficiencies / AR 0.7 / $H_2$ 2.0 / $H_2O$ 6.0 / $CH_4$ 2.0 / $C_2H_6$ 3.0 / CO 1.5 / $CO_2$ 2.0 / | | | | |
| 64 | $2CH_2 \rightleftharpoons H_2+C_2H_2$ | | 3.200E+13 | 0.000 | 0.000 |
| 65 | $H+CH_3(+M) \rightleftharpoons CH_4(+M)$ | $k_\infty$ | 1.270E+16 | -0.630 | 382.890 |
| | | $k_0$ | 2.48E+33 | -4.76 | 2440.0 |
| | $a_0 = 0.8422$ $a_1 = 125$ $a_2 = 2219$ $a_3 = 6882$ | | | | |
| | third-body efficiencies / AR 0.7 / $H_2$ 2.0 / $H_2O$ 6.0 / $CH_4$ 2.0 / $C_2H_6$ 3.0 / CO 1.5 / $CO_2$ 2.0 / | | | | |
| 66 | $2CH_3(+M) \rightleftharpoons C_2H_6(+M)$ | $k_\infty$ | 2.120E+16 | -0.970 | 619.980 |
| | | $k_0$ | 1.77E+50 | -9.67 | 6220.0 |
| | $a_0 = 0.8422$ $a_1 = 125$ $a_2 = 2219$ $a_3 = 6882$ | | | | |
| | third-body efficiencies / AR 0.7 / $H_2$ 2.0 / $H_2O$ 6.0 / $CH_4$ 2.0 / $C_2H_6$ 3.0 / CO 1.5 / $CO_2$ 2.0 / | | | | |
| 67 | $CH_3+O_2 \rightleftharpoons OH+CH_2O$ | | 3.600E+10 | 0.000 | 8940.010 |
| 68 | $OH+CH_3 \rightleftharpoons CH_2+H_2O$ | | 5.600E+07 | 1.600 | 5419.930 |
| 69 | $HO_2+CH_3 \rightleftharpoons O_2+CH_4$ | | 1.000E+12 | 0.000 | 0.000 |

| No | Reaction | | $A_n$ | $b_n$ | $E_n$ |
|---|---|---|---|---|---|
| 70 | $2CH_3 \rightleftharpoons H+C_2H_5$ | | 4.990E+12 | 0.100 | 10599.900 |
| 71 | $CH_2+CH_3 \rightleftharpoons H+C_2H_4$ | | 4.000E+13 | 0.000 | 0.000 |
| 72 | $O+CH_3 \rightleftharpoons H+CH_2O$ | | 8.430E+13 | 0.000 | 0.000 |
| 73 | $CH_3+H_2O_2 \rightleftharpoons HO_2+CH_4$ | | 2.450E+04 | 2.470 | 5179.970 |
| 74 | $OH+CH_3(+M) \rightleftharpoons CH_3OH(+M)$ | $k_\infty$ | 6.300E+13 | 0.000 | 0.000 |
| | | $k_0$ | 2.70E+38 | -6.30 | 3100.0 |
| | $a_0 = 0.8422$ $a_1 = 125$ $a_2 = 2219$ $a_3 = 6882$ | | | | |
| | third-body efficiencies / $H_2$ 2.0 / $H_2O$ 6.0 / $CH_4$ 2.0 / $C_2H_6$ 3.0 / CO 1.5 / $CO_2$ 2.0 / | | | | |
| 75 | $CH_3+O_2 \rightleftharpoons O+CH_3O$ | | 2.675E+13 | 0.000 | 28799.950 |
| 76 | $HO_2+CH_3 \rightleftharpoons OH+CH_3O$ | | 2.000E+13 | 0.000 | 0.000 |
| 77 | $CH_3CL \rightleftharpoons CH_3+CL$ | | 1.000E+16 | 0.000 | 84369.980 |
| 78 | $CH_3CL+CL \rightleftharpoons CH_3+CL_2$ | | 1.000E+14 | 0.000 | 25619.980 |
| 79 | $OH+CH_4 \rightleftharpoons CH_3+H_2O$ | | 1.000E+08 | 1.600 | 3119.980 |
| 80 | $CH_4+CL \rightleftharpoons CH_3+HCL$ | | 4.589E+11 | 2.490 | 1171.130 |
| 81 | $CH_2+CH_4 \rightleftharpoons 2CH_3$ | | 2.460E+06 | 2.000 | 8270.080 |
| 82 | $O+CH_4 \rightleftharpoons OH+CH_3$ | | 1.020E+09 | 1.500 | 8599.900 |
| 83 | $H+CH_4 \rightleftharpoons CH_3+H_2$ | | 6.600E+08 | 1.620 | 10840.110 |
| 84 | $O_2+CO \rightleftharpoons O+CO_2$ | | 2.500E+12 | 0.000 | 47799.950 |
| 85 | $H_2+CO(+M) \rightleftharpoons CH_2O(+M)$ | $k_\infty$ | 4.300E+07 | 1.500 | 79599.900 |
| | | $k_0$ | 5.07E+27 | -3.42 | 84350.0 |
| | $a_0 = 0.8422$ $a_1 = 125$ $a_2 = 2219$ $a_3 = 6882$ | | | | |
| | third-body efficiencies / AR 0.7 / $H_2$ 2.0 / $H_2O$ 6.0 / $CH_4$ 2.0 / $C_2H_6$ 3.0 / CO 1.5 / $CO_2$ 2.0 / | | | | |
| 86 | $CH_2+CO(+M) \rightleftharpoons CH_2CO(+M)$ | $k_\infty$ | 8.100E+11 | 0.500 | 4510.040 |
| | | $k_0$ | 2.69E+33 | -5.11 | 7095.0 |
| | $a_0 = 0.8422$ $a_1 = 125$ $a_2 = 2219$ $a_3 = 6882$ | | | | |
| | third-body efficiencies / AR 0.7 / $H_2$ 2.0 / $H_2O$ 6.0 / $CH_4$ 2.0 / $C_2H_6$ 3.0 / CO 1.5 / $CO_2$ 2.0 / | | | | |
| 87 | $OH+CO \rightleftharpoons H+CO_2$ | | 4.760E+07 | 1.228 | 70.030 |
| 88 | $HO_2+CO \rightleftharpoons OH+CO_2$ | | 1.500E+14 | 0.000 | 23599.900 |
| 89 | O+CO+M¡⇌ ¿$CO_2$+M | | 6.020E+14 | 0.000 | 3000.000 |
| | third-body efficiencies / AR 0.5 / $H_2$ 2.0 / $O_2$ 6.0 / $H_2O$ 6.0 / $CH_4$ 2.0 / $C_2H_6$ 3.0 / CO 1.5 / | | | | |
| 90 | $HCO+H_2O \rightleftharpoons H+CO+H_2O$ | | 2.244E+18 | -1.000 | 17000.000 |

| No | Reaction | | $A_n$ | $b_n$ | $E_n$ |
|---|---|---|---|---|---|
| 91 | H+HCO(+M)⇌ $CH_2O$(+M) | $k_\infty$ | 1.090E+12 | 0.480 | -260.040 |
| | | $k_0$ | 1.35E+24 | -2.57 | 1425.0 |
| | $a_0 = 0.8422$ $a_1 = 125$ $a_2 = 2219$ $a_3 = 6882$ | | | | |
| | third-body efficiencies / AR 0.7 / $H_2$ 2.0 / $H_2O$ 6.0 / $CH_4$ 2.0 / $C_2H_6$ 3.0 / CO 1.5 / $CO_2$ 2.0 / | | | | |
| 92 | H+HCO⇌ $H_2$+CO | | 7.340E+13 | 0.000 | 0.000 |
| 93 | O+HCO⇌ H+$CO_2$ | | 3.000E+13 | 0.000 | 0.000 |
| 94 | O+HCO⇌ OH+CO | | 3.000E+13 | 0.000 | 0.000 |
| 95 | HCO+M⇌ H+CO+M | | 1.870E+17 | -1.000 | 17000.000 |
| | third-body efficiencies / $H_2$ 2.0 / $H_2O$ 0.0 / $CH_4$ 2.0 / $C_2H_6$ 3.0 / CO 1.5 / $CO_2$ 2.0 / | | | | |
| 96 | OH+HCO⇌ $H_2O$+CO | | 5.000E+13 | 0.000 | 0.000 |
| 97 | $CH_3$+HCO⇌ $CH_4$+CO | | 2.648E+13 | 0.000 | 0.000 |
| 98 | HCO+$O_2$⇌ $HO_2$+CO | | 7.600E+12 | 0.000 | 400.100 |
| 99 | $O_2$+$CH_2O$⇌ $HO_2$+HCO | | 1.000E+14 | 0.000 | 40000.000 |
| 100 | H+$CH_2O$(+M)⇌ $CH_3O$(+M) | $k_\infty$ | 5.400E+11 | 0.454 | 2599.900 |
| | | $k_0$ | 2.20E+30 | -4.80 | 5560.0 |
| | $a_0 = 0.8422$ $a_1 = 125$ $a_2 = 2219$ $a_3 = 6882$ | | | | |
| | third-body efficiencies / $H_2$ 2.0 / $H_2O$ 6.0 / $CH_4$ 2.0 / $C_2H_6$ 3.0 / CO 1.5 / $CO_2$ 2.0 / | | | | |
| 101 | $CH_3$+$CH_2O$⇌ HCO+$CH_4$ | | 3.320E+03 | 2.810 | 5859.940 |
| 102 | OH+$CH_2O$⇌ HCO+$H_2O$ | | 3.430E+09 | 1.180 | -446.940 |
| 103 | O+$CH_2O$⇌ OH+HCO | | 3.900E+13 | 0.000 | 3539.910 |
| 104 | H+$CH_2O$⇌ HCO+$H_2$ | | 2.300E+10 | 1.050 | 3275.100 |
| 105 | H+$CH_2O$(+M)⇌ $CH_2OH$(+M) | $k_\infty$ | 5.400E+11 | 0.454 | 3599.900 |
| | | $k_0$ | 1.27E+32 | -4.82 | 6530.0 |
| | $a_0 = 0.8422$ $a_1 = 125$ $a_2 = 2219$ $a_3 = 6882$ | | | | |
| | third-body efficiencies / $H_2$ 2.0 / $H_2O$ 6.0 / $CH_4$ 2.0 / $C_2H_6$ 3.0 / CO 1.5 / $CO_2$ 2.0 / | | | | |
| 106 | $HO_2$+$CH_2O$⇌ HCO+$H_2O_2$ | | 1.000E+12 | 0.000 | 8000.000 |
| 107 | H+$CH_2OH$⇌ OH+$CH_3$ | | 1.200E+13 | 0.000 | 0.000 |
| 108 | H+$CH_2OH$(+M)⇌ $CH_3OH$(+M) | $k_\infty$ | 1.800E+13 | 0.000 | 0.000 |
| | | $k_0$ | 3.00E+31 | -4.80 | 3300.0 |
| | $a_0 = 0.8422$ $a_1 = 125$ $a_2 = 2219$ $a_3 = 6882$ | | | | |
| | third-body efficiencies / $H_2$ 2.0 / $H_2O$ 6.0 / $CH_4$ 2.0 / $C_2H_6$ 3.0 / CO 1.5 / $CO_2$ 2.0 / | | | | |
| 109 | O+$CH_2OH$⇌ OH+$CH_2O$ | | 1.000E+13 | 0.000 | 0.000 |
| 110 | H+$CH_2OH$⇌ $H_2$+$CH_2O$ | | 2.000E+13 | 0.000 | 0.000 |
| 111 | $CH_2OH$+$O_2$⇌ $HO_2$+$CH_2O$ | | 1.800E+13 | 0.000 | 900.100 |
| 112 | OH+$CH_2OH$⇌ $H_2O$+$CH_2O$ | | 5.000E+12 | 0.000 | 0.000 |

| No | Reaction | | $A_n$ | $b_n$ | $E_n$ |
|---|---|---|---|---|---|
| 113 | $H+CH_3O \rightleftharpoons OH+CH_3$ | | 3.200E+13 | 0.000 | 0.000 |
| 114 | $H+CH_3O \rightleftharpoons H+CH_2OH$ | | 3.400E+06 | 1.600 | 0.000 |
| 115 | $CH_3O+O_2 \rightleftharpoons HO_2+CH_2O$ | | 4.280E-13 | 7.600 | -3530.110 |
| 116 | $H+CH_3O(+M) \rightleftharpoons CH_3OH(+M)$ | $k_\infty$ | 5.000E+13 | 0.000 | 0.000 |
| | | $k_0$ | 8.60E+28 | -4.00 | 3025.0 |
| | $a_0 = 0.8422\ a_1 = 125\ a_2 = 2219\ a_3 = 6882$ | | | | |
| | third-body efficiencies / $H_2$ 2.0 / $H_2O$ 6.0 / $CH_4$ 2.0 / $C_2H_6$ 3.0 / CO 1.5 / $CO_2$ 2.0 / | | | | |
| 117 | $O+CH_3O \rightleftharpoons OH+CH_2O$ | | 1.000E+13 | 0.000 | 0.000 |
| 118 | $OH+CH_3O \rightleftharpoons H_2O+CH_2O$ | | 5.000E+12 | 0.000 | 0.000 |
| 119 | $H+CH_3O \rightleftharpoons H_2+CH_2O$ | | 2.000E+13 | 0.000 | 0.000 |
| 120 | $CH_3+CH_3OH \rightleftharpoons CH_3O+CH_4$ | | 1.000E+07 | 1.500 | 9940.010 |
| 121 | $H+CH_3OH \rightleftharpoons CH_2OH+H_2$ | | 1.700E+07 | 2.100 | 4869.980 |
| 122 | $OH+CH_3OH \rightleftharpoons CH_3O+H_2O$ | | 6.300E+06 | 2.000 | 1500.000 |
| 123 | $OH+CH_3OH \rightleftharpoons CH_2OH+H_2O$ | | 1.440E+06 | 2.000 | -840.110 |
| 124 | $O+CH_3OH \rightleftharpoons OH+CH_2OH$ | | 3.880E+05 | 2.500 | 3099.900 |
| 125 | $H+CH_3OH \rightleftharpoons CH_3O+H_2$ | | 4.200E+06 | 2.100 | 4869.980 |
| 126 | $CH_3+CH_3OH \rightleftharpoons CH_2OH+CH_4$ | | 3.000E+07 | 1.500 | 9940.010 |
| 127 | $O+CH_3OH \rightleftharpoons OH+CH_3O$ | | 1.300E+05 | 2.500 | 5000.000 |
| 128 | $2H+CO_2 \rightleftharpoons H_2+CO_2$ | | 5.500E+20 | -2.000 | 0.000 |
| 129 | $OH+C_2H_2 \rightleftharpoons CH_3+CO$ | | 4.830E-04 | 4.000 | -2000.000 |
| 130 | $O+C_2H_2 \rightleftharpoons H+HCCO$ | | 1.020E+07 | 2.000 | 1900.100 |
| 131 | $H+C_2H_2(+M) \rightleftharpoons C_2H_3(+M)$ | $k_\infty$ | 5.600E+12 | 0.000 | 2400.100 |
| | | $k_0$ | 3.80E+40 | -7.27 | 7220.0 |
| | $a_0 = 0.8422\ a_1 = 125\ a_2 = 2219\ a_3 = 6882$ | | | | |
| | third-body efficiencies / AR 0.7 / $H_2$ 2.0 / $H_2O$ 6.0 / $CH_4$ 2.0 / $C_2H_6$ 3.0 / CO 1.5 / $CO_2$ 2.0 / | | | | |
| 132 | $O+C_2H_2 \rightleftharpoons CO+CH_2$ | | 1.020E+07 | 2.000 | 1900.100 |
| 133 | $OH+C_2H_2 \rightleftharpoons H+CH_2CO$ | | 2.180E-04 | 4.500 | -1000.000 |
| 134 | $H+C_2H_3(+M) \rightleftharpoons C_2H_4(+M)$ | $k_\infty$ | 6.080E+12 | 0.270 | 280.110 |
| | | $k_0$ | 1.40E+30 | -3.86 | 3320.0 |
| | $a_0 = 0.8422\ a_1 = 125\ a_2 = 2219\ a_3 = 6882$ | | | | |
| | third-body efficiencies / AR 0.7 / $H_2$ 2.0 / $H_2O$ 6.0 / $CH_4$ 2.0 / $C_2H_6$ 3.0 / CO 1.5 / $CO_2$ 2.0 / | | | | |
| 135 | $O+C_2H_3 \rightleftharpoons H+CH_2CO$ | | 3.000E+13 | 0.000 | 0.000 |
| 136 | $C_2H_3+O_2 \rightleftharpoons HCO+CH_2O$ | | 3.980E+12 | 0.000 | -239.960 |
| 137 | $H+C_2H_3 \rightleftharpoons H_2+C_2H_2$ | | 3.000E+13 | 0.000 | 0.000 |

| No | Reaction | | $A_n$ | $b_n$ | $E_n$ |
|---|---|---|---|---|---|
| 138 | $OH+C_2H_3 \rightleftharpoons H_2O+C_2H_2$ | | 5.000E+12 | 0.000 | 0.000 |
| 139 | $CH_3+C_2H_4 \rightleftharpoons C_2H_3+CH_4$ | | 2.270E+05 | 2.000 | 9200.050 |
| 140 | $H+C_2H_4 \rightleftharpoons C_2H_3+H_2$ | | 1.325E+06 | 2.530 | 12239.960 |
| 141 | $C_2H_4(+M) \rightleftharpoons H_2+C_2H_2(+M)$ | $k_\infty$ | 8.000E+12 | 0.440 | 88770.080 |
| | | $k_0$ | 7.00E+50 | -9.31 | 99860.0 |
| | $a_0 = 0.8422\ a_1 = 125\ a_2 = 2219\ a_3 = 6882$ | | | | |
| | third-body efficiencies / AR 0.7 / $H_2$ 2.0 / $H_2O$ 6.0 / $CH_4$ 2.0 / $C_2H_6$ 3.0 / CO 1.5 / $CO_2$ 2.0 / | | | | |
| 142 | $OH+C_2H_4 \rightleftharpoons C_2H_3+H_2O$ | | 3.600E+06 | 2.000 | 2500.000 |
| 143 | $O+C_2H_4 \rightleftharpoons CH_3+HCO$ | | 1.920E+07 | 1.830 | 219.890 |
| 144 | $H+C_2H_4(+M) \rightleftharpoons C_2H_5(+M)$ | $k_\infty$ | 1.080E+12 | 0.454 | 1820.030 |
| | | $k_0$ | 1.20E+42 | -7.62 | 6970.0 |
| | $a_0 = 0.8422\ a_1 = 125\ a_2 = 2219\ a_3 = 6882$ | | | | |
| | third-body efficiencies / AR 0.7 / $H_2$ 2.0 / $H_2O$ 6.0 / $CH_4$ 2.0 / $C_2H_6$ 3.0 / CO 1.5 / $CO_2$ 2.0 / | | | | |
| 145 | $C_2H_5+O_2 \rightleftharpoons HO_2+C_2H_4$ | | 8.400E+11 | 0.000 | 3875.000 |
| 146 | $H+C_2H_5 \rightleftharpoons H_2+C_2H_4$ | | 2.000E+12 | 0.000 | 0.000 |
| 147 | $H+C_2H_5(+M) \rightleftharpoons C_2H_6(+M)$ | $k_\infty$ | 5.210E+17 | -0.990 | 1580.070 |
| | | $k_0$ | 1.99E+41 | -7.08 | 6685.0 |
| | $a_0 = 0.8422\ a_1 = 125\ a_2 = 2219\ a_3 = 6882$ | | | | |
| | third-body efficiencies / AR 0.7 / $H_2$ 2.0 / $H_2O$ 6.0 / $CH_4$ 2.0 / $C_2H_6$ 3.0 / CO 1.5 / $CO_2$ 2.0 / | | | | |
| 148 | $O+C_2H_5 \rightleftharpoons CH_3+CH_2O$ | | 1.320E+14 | 0.000 | 0.000 |
| 149 | $CH_3+C_2H_6 \rightleftharpoons C_2H_5+CH_4$ | | 6.140E+06 | 1.740 | 10450.050 |
| 150 | $H+C_2H_6 \rightleftharpoons C_2H_5+H_2$ | | 1.150E+08 | 1.900 | 7530.110 |
| 151 | $O+C_2H_6 \rightleftharpoons OH+C_2H_5$ | | 8.980E+07 | 1.920 | 5690.010 |
| 152 | $OH+C_2H_6 \rightleftharpoons C_2H_5+H_2O$ | | 3.540E+06 | 2.120 | 869.980 |
| 153 | $HCCO+O_2 \rightleftharpoons OH+2CO$ | | 1.600E+12 | 0.000 | 853.970 |
| 154 | $O+HCCO \rightleftharpoons H+2CO$ | | 1.000E+14 | 0.000 | 0.000 |
| 155 | $CH_2+HCCO \rightleftharpoons C_2H_3+CO$ | | 3.000E+13 | 0.000 | 0.000 |
| 156 | $2HCCO \rightleftharpoons 2CO+C_2H_2$ | | 1.000E+13 | 0.000 | 0.000 |
| 157 | $O+CH_2CO \rightleftharpoons OH+HCCO$ | | 1.000E+13 | 0.000 | 8000.000 |
| 158 | $H+CH_2CO \rightleftharpoons CH_3+CO$ | | 1.130E+13 | 0.000 | 3428.060 |
| 159 | $O+CH_2CO \rightleftharpoons CH_2+CO_2$ | | 1.750E+12 | 0.000 | 1349.900 |
| 160 | $H+CH_2CO \rightleftharpoons HCCO+H_2$ | | 5.000E+13 | 0.000 | 8000.000 |
| 161 | $OH+CH_2CO \rightleftharpoons HCCO+H_2O$ | | 7.500E+12 | 0.000 | 2000.000 |
| 162 | $H+O_2+N_2 \rightleftharpoons HO_2+N_2$ | | 3.750E+20 | -1.720 | 0.000 |

# Bibliography

[1] H. K. Kammler, L. Madler, and S. E. Pratsinis, "Flame synthesis of nanoparticles," *Chemical Engineering & Technology*, vol. 24, pp. 583–596, 2001.

[2] S. Consulting, "Chemical economics handbook," tech. rep., SRI Consulting, 2001.

[3] A. Teleki and S. Pratsinis, "Blue nano titania made in diffusion flames," *Physical Chemistry Chemical Physics*, vol. 11, pp. 3742–3747, 2009.

[4] A. Fujishima, "Discovery and applications of photocatalysis - creating a comfortable future by making use of light energy," *Japan Nanonet Bulletin*, vol. 44, 2005.

[5] P. Roth, "Particle synthesis in flames," *Proc. Combust. Inst.*, vol. 31, pp. 1773–1788, 2007.

[6] S. E. Pratsinis, W. Zhu, and S. Vemury, "The role of gas mixing in flame synthesis of titania powders," *Powder Technology*, vol. 86, pp. 87–93, 1996.

[7] E. Ukaji, T. Furusawa, M. Sato, and N. Suzuki, "The effect of surface modification with silane coupling agent on suppressing the photo-catalytic

activity of fine tio2 particles as inorganic uv filter," *Applied Surface Science*, vol. 254, no. 2, pp. 563–569, 2007.

[8] H. Wang, Z. Wu, W. Zhao, and B. Guan, "Photocatalytic oxidation of nitrogen oxides using tio2 loading on woven glass fabric," *Chemosphere*, vol. 66, pp. 185–190, 2007.

[9] L. Zhang, T. Kanki, N. Sano, and A. Toyoda, "Development of tio2 photocatalyst reaction for water purification," *Separation and Purification Technology*, vol. 31, no. 1, pp. 105–110, 2003.

[10] U. Bach, D. Lupo, P. Comte, J. Moser, F. Weissortel, J. Salbeck, H. Spreitzer, and M. Gratzel, "Solid-state dye-sensitized mesoporous tio2 solar cells with high photon-to-electron conversion efficiencies," *Nature*, vol. 395, pp. 583–585, 1998.

[11] I. Future Markets, "The world market for titanium dioxide nanopowders," tech. rep., Future Markets, Inc., 2010.

[12] S. E. Pratsinis, "Flame aerosol synthesis of ceramic powders," *Progress in Energy and Combustion Science*, 1998.

[13] O. I. Arabi-Katbi, S. E. Pratsinis, J. P. W. Morrison, and C. M. Megaridis, "Monitoring the flame synthesis of tio2 particles by in-situ ftir spectroscopy and thermophoretic sampling," *Combustion and Flame*, vol. 124, pp. 560–572, 2001.

[14] S. E. Pratsinis, H. Bai, P. Biswas, M. Frenklach, and S. V. R. Mastrangelo, "Kinetics of titanium(iv) chloride oxidation," *Journal of American Ceramic Society*, vol. 73, pp. 2158–2162, 1990.

[15] M. Mehta, Y. Sung, V. Raman, and R. O. Fox, "Multiscale modeling of tio2 nanoparticle production in flame reactors; effect of chemical mechanism," *Industrial Engineering Chemistry Research*, vol. 49, pp. 10663–10673, 2010.

[16] T. Johannessen, S. E. Pratsinis, and H. Livbjerg, "Computational analysis of coagulation and coalescence in the flame synthesis of titania particles," *Powder Technology*, vol. 118, pp. 242–250, 2001.

[17] P. T. Spicer, O. Chaoul, S. Tsantilis, and S. E. Pratsinis, "Titania formation by $TiCl_4$ gas phase oxidation, surface growth and coagulation," *Journal of Aerosol Science*, vol. 33, pp. 17–34, 2002.

[18] G. Wang and S. Garrick, "Modeling and simulation of titania synthesis in two-dimensional methane-air flames," *Journal of Nanoparticle Research*, vol. 7, pp. 621–632, 2005.

[19] M. Yu, J. Lin, and T. Chan, "Numerical simulation of nanoparticle synthesis in diffusion flame reactor," *Powder Technology*, vol. 181, pp. 9–20, 2008.

[20] R. H. West, G. J. O. Beran, W. H. Green, and M. Kraft, "Toward a comprehensive model of the synthesis of tio2 particles from ticl4," *Industrial*

*Engineering Chemistry Research*, vol. 46, pp. 6147–6156, 2007.

[21] R. H. West, R. A. Shirley, M. Kraft, and C. F. Goldsmith, "A detailed kinetic model for the combustion synthesis of titania from ticl4," *Combustion and Flame*, vol. 156, pp. 1764–1770, 2009.

[22] T. S. Totton, R. A. Shirley, and M. Kraft, "First-principles thermochemistry for the combustion of ticl4 in a methane flame," *Proceedings of Combustion Institute*, vol. 33, pp. 493–500, 2011.

[23] Y. Sung, V. Raman, and R. O. Fox, "Large-eddy-simulation-based multiscale modeling of tio2 nanoparticle synthesis in a turbulent flame reactor using detailed nucleation chemistry," *Chemical Engineering Science*, vol. 66, pp. 4370–4381, 2011.

[24] F. Bisetti, G. Blanquart, M. Mueller, and H. Pitsch, "On the formation and early evolution of soot in turbulent nonpremixed flames," *Combustion and Flame*, vol. 159, pp. 317–335, 2012.

[25] S. B. Pope, *Turbulent Flows*. Cambridge University Press, 2000.

[26] A. G. Kravchenko and P. Moin, "On the effect of numerical errors in large eddy simulations of turbulent flows," *Journal of Computational Physics*, vol. 131, pp. 310–322, 1997.

[27] M. M. Rogers and R. D. Moser, "Direct numerical simulation of a self-similar turbulent mixing layer," *Physics of Fluids*, vol. 6, pp. 903–923, 1994.

[28] P. Moin, *Fundamentals of Engineering Numerical Analysis.* Cambridge University Press, 2001.

[29] W. E. Stewart, M. Caracotsios, and J. P. Sorensen, "Ddasac software package documentation," 1994.

[30] I. Glassman and R. Yetter, *Combustion.* Academic Press, 2008.

[31] T. Passot and A. Pouquet, "Numerical-simulation of compressible homogeneous flows in the turbulent regime," *Journal of Fluid Mechanics*, vol. 1981, pp. 441–466, 1987.

[32] D. O. Lignell, J. H. Chen, P. J. Smith, T. Lu, and C. K. Law, "The effect of flame structure on soot formation and transport in turbulent nonpremixed flames using direct numerical simulation," *Combustion and Flame*, vol. 151, pp. 2–28, 2007.

[33] R. S. Rogallo and P. Moin, "Numerical simulation of turbulent flows," *Annual Reviews of Fluid Mechanics*, vol. 16, pp. 99–137, 1984.

[34] N. Peters, *Turbulent Combustion.* Cambridge University Press, 2000.

[35] R. O. Fox, *Computational Models for Turbulent Reacting Flows.* Cambridge University Press, 2003.

[36] H. Pitsch, "A C++ computer program for 0-d and 1-d laminar flame calculations." RWTH Aachen, 1998.

[37] J. Warnatz, U. Maas, and R. W. Dibble, *Combustion*. Berlin: Springer-Verlag, 1996.

[38] J. Kim, P. Moin, and R. D. Moser, "Turbulence statistics in fully developed channel flow at low Reynolds number," *Journal of Fluid Mechanics*, vol. 177, pp. 133–166, 1987.

# Vita

Ravi Ishwar Singh was born in Midland, Texas. He received the Bachelor of Science degree in Mechanical Engineering, with highest honors, from the University of Texas at Austin in December 2009. In January of 2010, he continued his studies at the University of Texas at Austin as a graduate student in the mechanical engineering department. During his first year, he served as a teaching assistant for ME 326 Thermodynamics under Dr. Philip Schmidt and Dr. Mark Deinert. In August of 2010, he joined Dr. Venkat Raman's Computational Flow Physics Group. He will graduate with a Master of Science in Mechanical Engineering in August 2012. He will continue his studies in September 2012, when he will join the Ph.D. program in Mechanical Engineering at the University of California Berkeley.

Email address: raviisingh@sbcglobal.net

This thesis was typeset with LaTeX[†] by the author.

[†]LaTeX is a document preparation system developed by Leslie Lamport as a special version of Donald Knuth's TeX Program.